

# Intrinsic dendritic filtering gives low-pass power spectra of local field potentials

Henrik Lindén · Klas H. Pettersen · Gaute T. Einevoll

Received: 31 August 2009 / Revised: 30 March 2010 / Accepted: 6 May 2010  
© Springer Science+Business Media, LLC 2010

**Abstract** The local field potential (LFP) is among the most important experimental measures when probing neural population activity, but a proper understanding of the link between the underlying neural activity and the LFP signal is still missing. Here we investigate this link by mathematical modeling of contributions to the LFP from a single layer-5 pyramidal neuron and a single layer-4 stellate neuron receiving synaptic input. An intrinsic dendritic low-pass filtering effect of the LFP signal, previously demonstrated for extracellular signatures of action potentials, is seen to strongly affect the LFP power spectra, even for frequencies as low as 10 Hz for the example pyramidal neuron. Further, the LFP signal is found to depend sensitively on both the recording position and the position of the synaptic input: the LFP power spectra recorded close to the active synapse are typically found to be less low-pass filtered than spectra recorded further away. Some recording positions display striking band-pass characteristics of

the LFP. The frequency dependence of the properties of the *current dipole moment* set up by the synaptic input current is found to qualitatively account for several salient features of the observed LFP. Two approximate schemes for calculating the LFP, the *dipole* approximation and the *two-monopole* approximation, are tested and found to be potentially useful for translating results from large-scale neural network models into predictions for results from electroencephalographic (EEG) or electrocorticographic (ECoG) recordings.

**Keywords** Local field potential · Single neuron · Forward modeling · Frequency dependence · EEG

## 1 Introduction

Extracellular recordings have been, and still are, among the most used methods for probing neural activity. This popularity mainly stems from the spike-counting abilities of sharp electrodes: when placed sufficiently close to a particular neuronal soma, such electrodes will measure a sequence of standardized extracellular potential signatures, each signalling the presence of an action potential in that particular neuron. Information about spiking is commonly extracted from the high frequency band ( $\gtrsim 500$  Hz) of the recorded extracellular potentials. The interpretation of the *local field potential (LFP)*, i.e., the low-frequency part ( $\lesssim 500$  Hz) of extracellular potentials, is generally not so straightforward. The LFP appears to be dominated by dendritic processing of synaptic inputs, not firing of action potentials (Nunez and Srinivasan 2006; Einevoll et al. 2007; Pettersen et al. 2008), and the LFP measured at any

---

**Action Editor: Abraham Zvi Snyder**

H. Lindén · K. H. Pettersen · G. T. Einevoll  
Department of Mathematical Sciences and Technology,  
Norwegian University of Life Sciences,  
PO Box 5003, 1432, Ås, Norway

H. Lindén  
e-mail: Henrik.Linden@umb.no

K. H. Pettersen  
e-mail: Klas.Pettersen@umb.no

G. T. Einevoll (✉)  
Center for Integrative Genetics,  
Norwegian University of Life Sciences,  
Ås, Norway  
e-mail: Gaute.Einevoll@umb.no

point will have sizable contributions from neurons located many hundred micrometers away (Kreiman et al. 2006; Liu and Newsome 2006; Berens et al. 2008; Lindén et al. 2008, 2009a; Katzner et al. 2009; Xing et al. 2009).

The advent of new silicon-based multicontact electrical probes in various geometrical arrangements, such as ‘multi-shank’ (Buzsáki 2004) or ‘needlepad’ (Normann et al. 1999), offers new exciting opportunities for massively parallel recordings of LFP. Thus LFP certainly has the potential of becoming one of the most important experimental measures when probing neural *population* activity (Mitzdorf 1985; Arieli 1992; Di et al. 1990; Einevoll et al. 2007; Kreiman et al. 2006; Nauhaus et al. 2009). This will require, however, a substantial improvement in our understanding of the link between the underlying activity in neurons and the recorded LFP signal. The present model study aims to add to this understanding by investigating the contribution to the LFP signal from individual neurons receiving synaptic stimulation. Due to the linearity of electromagnetism, a recorded LFP signal will be built up by a linear sum of such contributions from individual neurons located in the vicinity of the electrode contact. The insight gained by studying the LFP signals generated by individual neurons will thus be of great help when embarking on the larger project of linking measured LFPs to activity in populations of neurons or comprehensive neural networks (Lindén et al. 2009a, b).

In the present study we particularly address the question on the origin of observed frequency spectra in LFP and EEG (electroencephalography) recordings (Pritchard 1992; Freeman et al. 2003; Bedard et al. 2006b; Buzsáki 2006; Bedard and Destexhe 2009; Milstein et al. 2009; Miller et al. 2009). In Pettersen and Einevoll (2008) we described an unavoidable low-pass frequency-filtering effect of the extracellular action-potential signature due to the electrical cable properties of the neuronal dendrites. In the present paper we find for our example layer-5 pyramidal neuron that the same intrinsic dendritic filtering effect also strongly affects frequencies down to about 10 Hz, i.e., well into the typical LFP and EEG frequency bands. Moreover, we find the detailed frequency-filtering effects to vary strongly with recording position: for apical synaptic stimulation the low-pass filtering effects are most prominent for recording positions near the soma, and vice versa. We also consider a spatially more compact layer-4 stellate neuron. The same low-pass filtering effect is observed, although with a higher cut-off frequency than for the spatially more extended layer-5 pyramidal neuron.

The use of dipole and other multipole moments in the modeling of bioelectric signals has a long his-

tory (Plonsey 1969; Plonsey and Barr 2007). The *current dipole* concept has been particularly important in the interpretation of EEG signals, but there one has typically considered ‘mesoscopic’ current dipoles representing the collective effect from large number of activated neurons (Nunez and Srinivasan 2006). In a recent study, however, we found the current dipole moment from a *single* neuron to be a very useful concept for gaining thorough understanding of the characteristics of extracellular signatures of action potentials (Pettersen and Einevoll 2008). Likewise, we here find the concept to be very useful for obtaining better understanding of the results from our numerically comprehensive calculations of LFPs generated by synaptic activation of individual neurons with complex dendritic morphologies. Further, used in combination with the standard far-field dipole approximation from electrostatics (Jackson 1998; Plonsey and Barr 2007), this quantity is even found to provide quantitatively accurate predictions of the LFP a millimeter or more away from the neuron. This dipole approximation, as well as a *two-monopole* approximation also explored here (Freeman 1980), may even find its use in ambitious large-scale neural network modeling schemes aspiring to predict results from EEG recordings or ECoG recordings, i.e., recordings done at the cortical surface.

Preliminary results from this project were presented earlier in poster format (Lindén et al. 2008).

## 2 Methods

### 2.1 Forward modeling of extracellular potentials

Extracellular potentials are generated by transmembrane currents, and in the presently used *volume conductor theory* the system is envisioned as a 3-dimensional smooth extracellular continuum with the transmembrane currents represented as *volume current sources* (Nunez and Srinivasan 2006). In volume conductor theory the fundamental formula for the contribution to the extracellular potential  $\phi(\mathbf{r}, t)$  from the activity in an  $N$ -compartment neuron model is given by (Nicholson and Freeman 1975; Holt and Koch 1999; Pettersen and Einevoll 2008; Pettersen et al. 2008)

$$\phi(\mathbf{r}, t) = \frac{1}{4\pi\sigma} \sum_{n=1}^N \frac{I_n(t)}{|\mathbf{r} - \mathbf{r}_n|}. \quad (1)$$

Here  $I_n(t)$  denotes the transmembrane current in compartment  $n$  positioned at  $\mathbf{r}_n$ , and  $\sigma$  is the extracellular conductivity. This formula relies on a set of assumptions and approximations: The first is the use of the

*quasistatic approximation* of Maxwell’s equations. This amounts to neglecting the terms with time derivatives of the electric field  $\mathbf{E}$  and magnetic field  $\mathbf{B}$  from the original Maxwell’s equations so that the electromagnetic field effectively decouples into separate ‘quasistatic’ electric and magnetic fields (Hämäläinen et al. 1993). Then the electric field  $\mathbf{E}$  in the extracellular medium is related to the extracellular potential  $\phi$  via  $\mathbf{E} = -\nabla\phi$ . For frequencies inherent in neural activity, i.e., less than a few thousand hertz, the quasistatic approximation seems to be well fulfilled (Hämäläinen et al. 1993).

Further, the formula assumes an infinite volume conductor where the electrical properties of the extracellular medium are assumed to be (1) *linear* and *frequency independent* (Logothetis et al. 2007), i.e.,  $\mathbf{j} = \sigma\mathbf{E}$  where  $\mathbf{j}$  is the current density, (2) *ohmic*, i.e., no imaginary part of  $\sigma$  (Nunez and Srinivasan 2006; Logothetis et al. 2007), (3) *position-independent*, i.e.,  $\sigma$  is the same everywhere, and (4) *isotropic*, i.e., same  $\sigma$  in all directions (Logothetis et al. 2007). For a more comprehensive discussion of these assumptions regarding the extracellular medium see Pettersen et al. (2010).

In a numerical scheme based on compartmental neuron models, the formula in Eq. (1) can be used directly with the position  $\mathbf{r}_n$  set to correspond to a characteristic ‘mean’ position of compartment  $n$ , e.g., the center of a spherical soma compartment or the mid-point of a cylindrical dendritic compartment. This scheme corresponds to the so called *point-source* approximation since all transmembrane currents leaving or entering the extracellular medium from a particular compartment are assumed to go through a single point (Holt and Koch 1999; Pettersen and Einevoll 2008). Another scheme, the *line-source* approximation, assumes the transmembrane currents from each cylindrical compartment to be evenly distributed along a line corresponding to the cylinder axis (Holt and Koch 1999; Pettersen and Einevoll 2008; Pettersen et al. 2008). A line-source formula, analogous to the point-source formula in Eq. (1), can be found in Eq. (2) of Pettersen and Einevoll (2008). All forward-modeling calculations presented in this paper use the line-source approximation with the extracellular conductivity set to  $\sigma = 0.3 \text{ S/m}$  (Hämäläinen et al. 1993).

## 2.2 Compartmental neuron modeling

All simulations were carried out using the NEURON simulation environment (Carnevale and Hines 2006) which was controlled via a Python interface (Hines et al. 2009). We used two different reconstructed cell morphologies, a layer-5 pyramidal cell and a layer-

4 stellate cell from cat visual cortex (Mainen and Sejnowski 1996), both downloaded from *ModelDB* at <http://senselab.med.yale.edu/>. To assure sufficient numerical precision the length of each compartment of the model neurons was chosen to be maximum one tenth of the electrotonic length at 100 Hz. This gave a total of 1,072 compartments for the layer-5 cell and 343 compartments for the layer-4 cell for our default choice of passive membrane parameters (see below). Simulations in NEURON were performed at a time resolution of 0.0625 ms. The default passive membrane parameters of the cell models were: specific membrane resistance  $R_m=30 \text{ k}\Omega \text{ cm}^2$ , specific axial resistance  $R_a=150 \text{ }\Omega \text{ cm}$ , and specific membrane capacitance  $C_m=1.0 \text{ }\mu\text{F/cm}^2$  (Mainen and Sejnowski 1996). In the testing of the dependence of LFP power spectra on model parameters we also considered specific membrane resistances  $R_m$  and specific axial resistances  $R_a$  corresponding to 1/10 and 10 times the default values.

In one application the synaptic input current  $I_s(t)$  was modeled as an  $\alpha$ -function, that is,

$$I_s(t) = I_0 \frac{t}{\tau_s} e^{1-t/\tau_s} \theta(t) \quad , \quad (2)$$

where  $\theta(t)$  is the Heaviside unit step function. Note that an excitatory synaptic input corresponds to a negative value of the current amplitude  $I_0$ . Simulations with this stimulus was run for 100 ms prior to onset of the  $\alpha$ -current to avoid any possible inaccuracies from up-start effects.

The input currents used for calculating LFP power spectra were created as a sum of sinusoidal currents,

$$I_s(t) = I_0 \sum_{f=1}^{1000} \sin(2\pi ft + \gamma_f) \quad (3)$$

where  $\gamma_f$  represents a random phase for each frequency contribution. This current contains all frequencies between 1 Hz and 1,000 Hz in steps of 1 Hz, has a flat frequency spectrum, and is for the purpose of this study equivalent to a ‘white-noise’ input current. The simulations were run for 1,200 ms. The calculated LFP signals from the last 1,000 ms were used in the evaluation of the power spectra which were obtained by squaring the Fourier amplitudes of the calculated LFP for each frequency.

Since the cable equation describing the present passive neuron is linear, the assumption of current synapses and passive neuronal membrane model makes the overall model linear. This means that all calculated extracellular and intracellular potentials will be proportional to the current amplitude  $I_0$ . Further, in the case of a sinusoidal input current, all extracellular

and intracellular potentials will also be sinusoidally oscillating with the same frequency, although in general with a different phase. The linearity of the model makes it easier to analyze. However, we expect that most of the observed qualitative features would remain if we, e.g., instead had considered excitation by conductance-based synapses.

### 2.3 Current dipole moments

Current dipole moments in the  $x$ -,  $y$ -, and  $z$ -directions were calculated as follows:

$$\begin{aligned}
 p_x(t) &= \sum_{n=1}^N x_n I_n(t), & p_y(t) &= \sum_{n=1}^N y_n I_n(t), \\
 p_z(t) &= \sum_{n=1}^N z_n I_n(t). & &
 \end{aligned}
 \tag{4}$$

where  $x_n$ ,  $y_n$ , and  $z_n$  are the  $x$ ,  $y$  and  $z$  positions of compartment  $n$ . When the synaptic input current is sinusoidal, i.e.,  $I_s(t) = I_0 \sin(2\pi ft)$ , these dipole moments will due to the linearity of the system be of the form

$$\begin{aligned}
 p_x(t) &= p_{0x}(f) \sin(2\pi ft + \gamma_{fx}), \\
 p_y(t) &= p_{0y}(f) \sin(2\pi ft + \gamma_{fy}), \\
 p_z(t) &= p_{0z}(f) \sin(2\pi ft + \gamma_{fz}).
 \end{aligned}
 \tag{5}$$

In the special case when the phases are identical, i.e.,  $\gamma_{fx} = \gamma_{fy} = \gamma_{fz} \equiv \gamma_f$ , the system simplifies to a sinusoidally oscillating dipole along a *fixed axis*,

$$\mathbf{p}_{fa}(t) = \mathbf{p}_0(f) \sin(2\pi ft + \gamma_f)
 \tag{6}$$

where  $\mathbf{p}_0(f)$  is a frequency-dependent vector given by

$$\mathbf{p}_0(f) \equiv p_{0x}(f)\mathbf{e}_x + p_{0y}(f)\mathbf{e}_y + p_{0z}(f)\mathbf{e}_z.
 \tag{7}$$

(Note that the system also reduces to a fixed-axis oscillating dipole when one of  $\gamma_{fx}$ ,  $\gamma_{fy}$ , or  $\gamma_{fz}$  is off by a factor  $\pi$  compared to the two others; then the factor  $\pi$  can be eliminated by changing the sign of the ‘amplitude’ in front of the particular sinus function.)

In the application of the dipole approximation for LFP generation in Sections 3.5 and 3.6 we assume the phases of the three cartesian dipole-moment components to be the same (modulo a factor  $\pi$ ) so that a linear dipole is obtained. In order to specify the direction of this linear dipole, one also has to decide the directions of the three components relative to each other. Here we set these directions, for all frequencies considered, to correspond to the current-dipole component directions found in the low frequency limit (1 Hz). With such slowly oscillating input currents the phase shifts between the dipole components are negligible, and the

assignment of directions follows directly from evaluating the sign of, say, the  $x$  and  $y$  components of the current dipole at the first peak for the  $z$  component.

## 3 Results

### 3.1 Example local field potentials

In Fig. 1 we show examples of patterns of extracellular potential traces around reconstructed neurons. These extracellular potentials are generated by single synaptic inputs for various synaptic positions and neuronal dendritic morphologies. The synaptic input currents are in all examples chosen as  $\alpha$ -functions (cf. Eq. (2)) with a time constant of 2 ms and a peak amplitude of 1 nA. In the following we will denote such synaptically generated extracellular potentials as *local field potentials (LFPs)*.

In Fig. 1(a) we show results for a reconstructed layer-5 pyramidal neuron, taken from Mainen and Sejnowski (1996), receiving a single excitatory synaptic input at an apical branch. The form of the injected synaptic current is illustrated by the inset panel. An important feature which is immediately apparent is that the shape and amplitude of the LFPs depend strongly on the recording position. Near the apical synaptic input the LFP signature is generally negative, reflecting that the excitatory current synapse providing a current sink dominates the sum in the forward-model formula, cf. Eq. (1). At positions close to the soma the LFP is always positive, reflecting that return currents in the soma area dominate the sum.

This characteristic dipolar structure is further illustrated by the contour plots shown in the figures as grey solid and dashed lines. These logarithmic contour plots show how the maximum value for LFP signal amplitude, i.e., maximum positive or negative deviation of LFP from baseline following the synaptic input, varies with position. For spatial positions above and to the left of the synaptic input in Fig. 1(a), this largest deviation corresponds to a negative LFP peak, and the dashed contour lines in this region thus corresponds to ‘equi-LFP’ lines with negative numerical values of the LFP. For spatial positions around the soma, positive LFP peaks dominate, and the solid contour lines correspondingly represent ‘equi-LFP’ lines with positive values of the LFP. Regardless of the sign of the maximum LFP amplitude, we generally observe a rapid decay of the LFP signal amplitude with distance: when moving away from the neuron, each new contour line represents a reduction of the LFP amplitude by a factor two compared to the previous contour line.

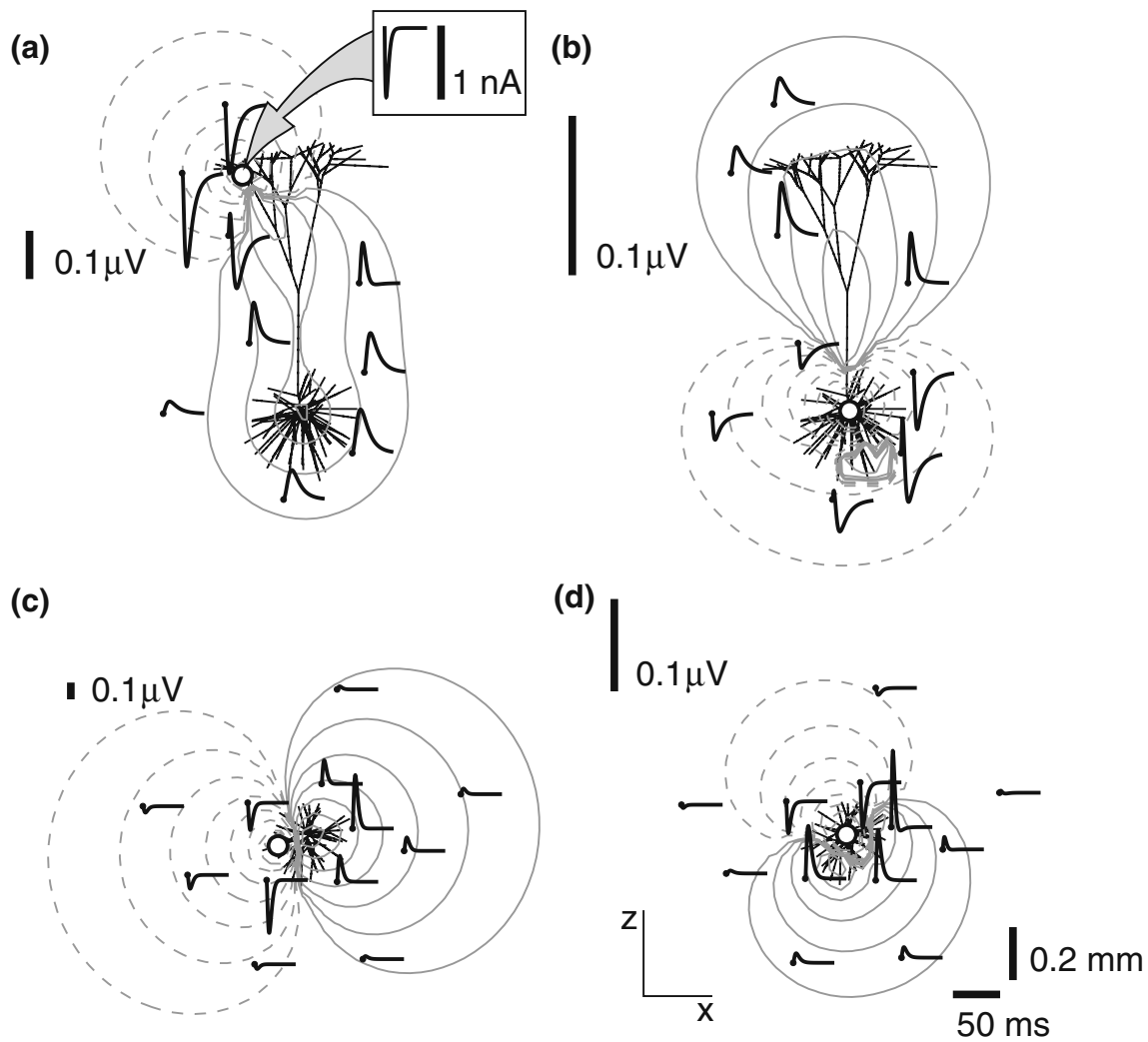


**Fig. 1** Examples of calculated local field potentials (LFPs) following an excitatory synaptic input into purely passive neuron models. The synapse is current-based and modeled as an  $\alpha$ -function (Eq. (2)) with an amplitude of 1 nA, i.e.,  $I_0 = -1$  nA, and a time constant  $\tau_s = 2$  ms; see panel inset in (a) for illustration of synaptic current. Neuron models are passive with the following specific electric parameters: membrane resistivity  $R_m = 30$  k $\Omega$  cm<sup>2</sup>, axial resistivity  $R_i = 150$   $\Omega$  cm, membrane capacitance  $C_m = 1$   $\mu$ F/cm<sup>2</sup>. Extracellular potentials (*thick solid lines*) at selected spatial positions (marked with dots on trace starting points) are shown in 50 ms windows. Grey contour lines illustrate maximal extracellular potential (LFP) amplitudes, i.e., maximum positive or negative deviation of LFP from baseline following the synaptic input. Contour plots are logarithmic and

based on  $\log_2$ , i.e., the LFP amplitude decays by a factor 2 between each contour line. Solid contour lines are ‘equi-LFP’ lines corresponding to positive values for the LFP amplitude, dashed contour lines to negative values of the LFP amplitude. (a) Results for reconstructed L5 pyramidal neuron (*solid branch structure*) from Mainen and Sejnowski (1996) with single excitatory synapse (*solid dot*) on apical branch. The neuron has been rotated so that both the synapse and soma are in the 2D plane of the plot. (b) Corresponding results as in (a) for a single excitatory synapse in soma. (c) Results for reconstructed L4 stellate neuron from Mainen and Sejnowski (1996) with single excitatory synapse on distal branch. (d) Corresponding results for a single excitatory synapse in soma

An excitatory synaptic input onto the *basal* dendrites of the pyramidal neuron will typically give the opposite pattern: negative LFPs around the basal synaptic input and positive LFPs around the apical dendrites (results not shown). However, due to the asymmetric dendritic branching with a dominant apical dendrite, even an excitatory input onto the soma gives a prominent dipolar

spatial pattern for the extracellular potentials. This is demonstrated in Fig. 1(b). Here we show results from injecting the same current used in Fig. 1(a) into the soma instead of into the apical synapse, and a spatial LFP pattern similar to what might be expected for an excitatory basal input is indeed observed. In Fig. 1(b), however, we see that the amplitudes of the LFP signal

are generally much smaller than for the situation with apical excitation depicted in Fig. 1(a). A qualitative explanation is that presumably more of the injected synaptic current returns to the extracellular medium closer to the injection point in the case with somatic input, than for input onto the apical dendrite. There will thus be more cancelation of the contributions from the various terms in the sum in Eq. (1).

A close inspection of the equipotential contour lines in Fig. 1(b) reveals a deviation from the simple dipolar pattern. In a region inside the basal dendritic tree just below the soma, the LFP signals with the largest magnitudes are seen to be positive, not negative as expected from the dipolar structure. In this region the early positive peak prominently seen in the potential trace to the right of and below the soma, has a larger magnitude than the peak of the following negative LFP signal. If we instead had plotted equipotential contour lines for the dominant, i.e., late, LFP peak, a clean dipolar pattern would have been seen.

The layer-5 pyramidal neuron in Fig. 1(a) and (b) has a characteristic ‘open-field’ dendritic structure where the synaptic input currents and the bulk of the return currents may be substantially separated in space (Johnston and Wu 1995). This will imply a sizable current dipole and, in turn, a sizable contribution to the experimentally recorded LFPs. For example, in panel (a) the distance between the position of the apical synaptic input and the soma, where a large part of the return current exits, is about a millimeter.

In Fig. 1(c) and (d) we show corresponding results for a layer-4 stellate neuron where the dendritic structure has a spherically symmetric appearance, implying a more ‘closed-field’ structure (Lorente de N6 1947; Rall 1962; Johnston and Wu 1995). As shown in panel (c), a distal synaptic input onto a dendritic branch will nevertheless produce a dipolar LFP pattern around the stellate neuron where the dipole axis will be oriented along a line between the synaptic input and the soma. Only when the set of distal inputs are distributed symmetrically around the soma can significant cancelation effects on the resulting LFP be expected. However, the cancelation can never be expected to be complete due to unavoidable asymmetry in the dendritic structure. The dendritic asymmetry as seen from the soma for the present stellate neuron is illustrated in Fig. 1(d) where the LFP pattern following a synaptic input into the soma is shown. Also for this situation a dipolar pattern of LFPs is observed, albeit generally with reduced amplitudes compared to the distal-excitation situation in (c). A comprehensive investigation of the dependence of sizes and shapes of the LFP patterns on the neuronal morphologies and synaptic input positions is beyond

the scope of the present paper, but the results in Fig. 1 caution us that one must be careful before a priori neglecting contributions to experimentally recorded LFP from populations of neurons with stellate dendritic structures.

Close inspection of Fig. 1(a) reveals another qualitative feature: the LFP signals close to the synaptic inputs positions have ‘narrower’ temporal traces compared to signals further away. In other words, the LFPs recorded close to the synaptic inputs have more power at higher temporal frequencies than LFPs recorded further away. This position-dependent temporal filtering of the LFP is also revealed by the shift in the times of the peaks of negative LFPs compared to the peak times for the positive LFPs in Fig. 1(a): we find, for example, that the peak of the purely negative LFP trace depicted immediately above the synaptic current-injection point, occurs 5 ms before the maximum of the purely positive LFP trace depicted immediately below the soma. This effect may at least partially underlie observed asynchronous positive and negative peaks of LFPs found in depth-resolved intracortical recordings in humans; in Fig. 2 in Godey et al. (2001) the negative LFP peak at around 45 ms in electrode H’1 is, for example, seen to occur about 5 ms prior to the positive LFP peak seen in electrode H’3.

This intrinsic dendritic filtering effect is a generic and unavoidable feature of spatially extended neuronal structures (Pettersen and Einevoll 2008), but the detailed characteristics of it will be determined by dendritic morphology, electrical cable properties of the dendrites, positions of the current-injecting synapses, as well as the recording position.

### 3.2 LFP power spectra depend on recording positions

In Fig. 2 we show calculated LFP power spectra, i.e., the square of Fourier amplitudes, for extracellular potentials in the frequency range between 1 and 1,000 Hz. Note the double-logarithmic axes. The same passive layer-5 pyramidal neuron as in the upper panels of Fig. 1 is considered, and we show LFP power spectra found from white-noise current injection (Eq. (3)) into the position of the synapse on the apical branch in Fig. 1(a). For easy comparison we have also drawn lines corresponding to  $1/f$  and  $1/f^2$  power laws of the LFP in an auxiliary panel.

An immediate observation is that the shape of the spectra is very different at the different recording positions and consequently that no general power-law behavior of the LFP spectra is found. The highest frequencies are to a large extent retained at positions close to the synaptic input, where the frequency at which

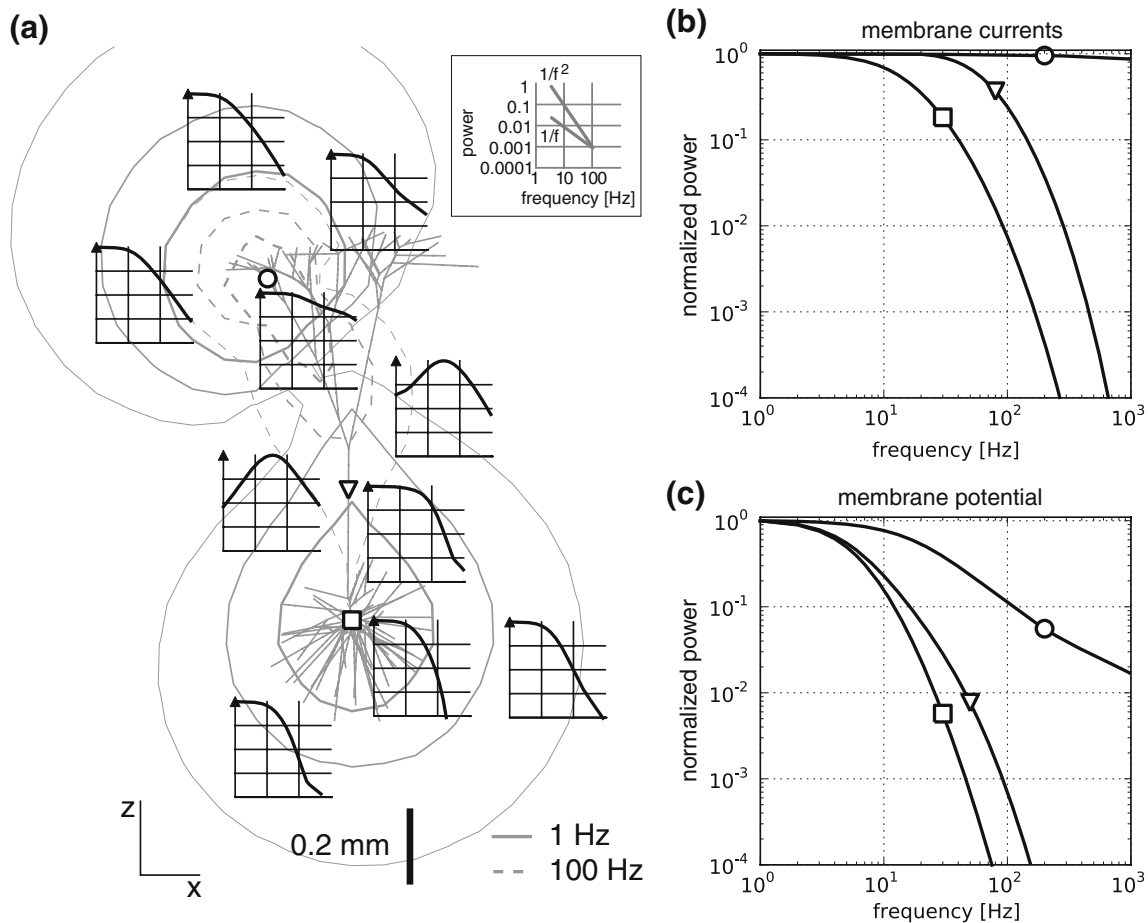


**Fig. 2** (a) Calculated power spectra of local field potentials (LFPs) following injection of white-noise current into a purely passive layer-5 pyramidal neuron (*grey solid branch structure*) from Mainen and Sejnowski (1996). The current injection point on the apical branch is marked with a circle. Same passive parameters as in Fig. 1. Doubly logarithmic power spectra in the frequency range 1–1,000 Hz of extracellular potentials (*thick solid lines*) are shown at selected spatial positions (*marked by filled arrows*). The power spectra are normalized to the maximum value in the range 1–1,000 Hz. See separate legend box in the upper right part of panel (a) for description of the logarithmic frequency

and power axes. Logarithmic contour plot with *grey solid lines* illustrate the decay of the 1-Hz power, i.e., square of Fourier amplitude, of the extracellular potential with distance from neuron. The power decays by a factor 4 between each contour line. *Grey dashed contour lines* correspondingly illustrate the decay of the 100-Hz power. (b) Normalized doubly-logarithmic power spectra of transmembrane currents at three different positions (synaptic current-injection point, circle; intermediate position, triangle; soma, square) marked with corresponding symbols in (a). (c) Same as (b), but for membrane potential

the power is reduced to one hundredth, is seen to be substantially above 100 Hz. In fact, the position immediately below the synaptic input shows a very modest low-pass filtering effect, and the power at 1,000 Hz is still as large as one tenth of the 1 Hz amplitude. The low-pass filtering effect is seen to be much stronger at the recording position closest to the soma where the ‘one-hundredth cut-off frequency’ is seen to be slightly less than 100 Hz. At some positions outside the main stalk of the apical dendrite one even observes a striking band-pass effect: the largest LFP power is found for frequencies between 10 and 100 Hz.

The above observations can be qualitatively understood by inspection of the corresponding power spectra of the membrane currents in Fig. 2(b). The membrane current at the synaptic injection point has by construction a flat (white-noise) spectrum (marked with a circle), and LFPs recorded in the vicinity of this current-injection point will thus retain substantial contributions from high frequencies. Due to the passive electrical properties of the dendritic cable structure, the somatic membrane current will be low-pass filtered as seen in the power spectrum for the soma (marked with a square). LFPs recorded in the vicinity of the soma

will be dominated by this soma membrane current and will thus exhibit similar power spectra. This is indeed confirmed by visual comparison with the power spectra of the LFPs recorded closest to the soma which shows essentially the same power spectrum.

The membrane current at the intermediate position on the dominant apical dendrite (marked with a triangle) has a smaller low-pass filtering effect compared to the soma membrane current, and the low-pass filtering effect of the LFPs recorded in the vicinity of this point is correspondingly smaller as well. Here a somewhat poorer agreement between the LFP spectrum and the corresponding membrane-current spectrum is observed. This reflects that the membrane area, and thus membrane current, around this intermediate position is small compared to both the basal and apical dendritic regions. Thus the recorded LFP signal will get significant contributions from the apical and basal parts of the dendritic tree, and the LFP power spectrum will be determined by a mixture of membrane-current contributions.

For comparison we also show in Fig. 2(c) the power spectra for the membrane *potential* at the same three positions on the pyramidal neuron. A much stronger low-pass filtering effect is observed for the membrane potentials compared to the membrane currents. Since the LFPs are determined by a weighted sum over membrane currents and not membrane potentials, the membrane potential is expected to be a poor predictor of the LFP. This is indeed confirmed by comparison of the power spectra of the membrane potential and the LFPs.

### 3.3 LFP power spectra depend on synaptic position, neuronal morphology and neuron parameters

In Fig. 3(a) we show the corresponding LFP power spectra for the situation where the synapse is at the soma of the layer-5 neuron instead of at an apical branch, cf. Fig. 1(b). Here the situation is reversed compared to Fig. 2(a): a strong low-pass filtering effect is now seen at the recording positions outside the apical dendrite, while the high frequencies are to a large extent retained at the recording position immediately outside the soma. This confirms the rule that LFP power spectra will exhibit less low-pass filtering close to the synaptic input position than further away (in analogy with the observation in Pettersen and Einevoll (2008) that the extracellular spike signature will become more low-pass filtered when moving away from soma).

In Fig. 3(b) we show LFP power spectra for the layer-4 stellate neuron receiving synaptic input at a distal part of a dendrite, in analogy to Fig. 1(c). Also here we

see prominent low-pass filtering effects, although with a higher cut-off frequency and less variation of power spectra with recording positions compared to the layer-5 neuron. This illustrates that the dendritic morphology of the neuron strongly affects their contribution to the LFP signal, and in particular that the length of the dendrites is an important parameter determining the frequency dependence of the intrinsic dendritic filtering (Pettersen and Einevoll 2008).

While Figs. 2 and 3 together illustrate the strong dependence of the intrinsic dendritic filtering effect of the LFP on recording position, synaptic input position and dendritic morphology, Fig. 4 illustrates how this filtering effect is affected by the passive electrical parameters in the neuron model. To highlight the qualitative effects we look at the extreme and likely unrealistic situations where the specific membrane resistance  $R_m$  and specific axial resistance  $R_a$  are increased or reduced by an order of magnitude compared to the default parameter values.

In Fig. 4(a) and (b) we show how the power spectra shown in Fig. 2(a) for the layer-5 neuron with apical synaptic input are changed when  $R_m$  is reduced (Fig. 4(a)) or increased (Fig. 4(b)) by a factor ten, respectively, compared to the default value  $R_m=30$  k $\Omega$  cm<sup>2</sup> used in Fig. 2(a). In Fig. 4(a) where the membrane resistance  $R_m$  is reduced by a factor ten, we see that the low-pass cut-off frequencies are shifted to higher values compared to the results for the default parameters in Fig. 2(a). This can be qualitatively understood since the reduction of the membrane resistance implies a corresponding reduction of the membrane time constant  $\tau_m = R_m C_m$  by a factor ten. This in turn implies that the characteristic frequencies of the system, such as low-pass cut-off frequencies, will be increased. We also observe that the characteristic band-pass spectra for positions outside the apical dendritic stalk in Fig. 2(a) is absent in Fig. 4(a). This illustrates that this resonance-like phenomenon depends on a detailed interplay between the neuronal morphology and its electrical cable properties. The inverse relationship between the membrane resistance  $R_m$ , and thus membrane time constant  $\tau_m$ , and the characteristic frequencies of the system is further illustrated by observations of the depicted spatial pattern of equipotential contour lines in Fig. 4(a). For this reduced membrane-resistance case the 100-Hz contour line is much more spatially extended and thus similar to the 1-Hz contour lines, than for the default situation in Fig. 2(a).

The opposite effect is observed in Fig. 4(b) where the specific membrane resistance is increased by a factor ten, and the typical cut-off frequencies as expected are shifted towards smaller values compared to the default

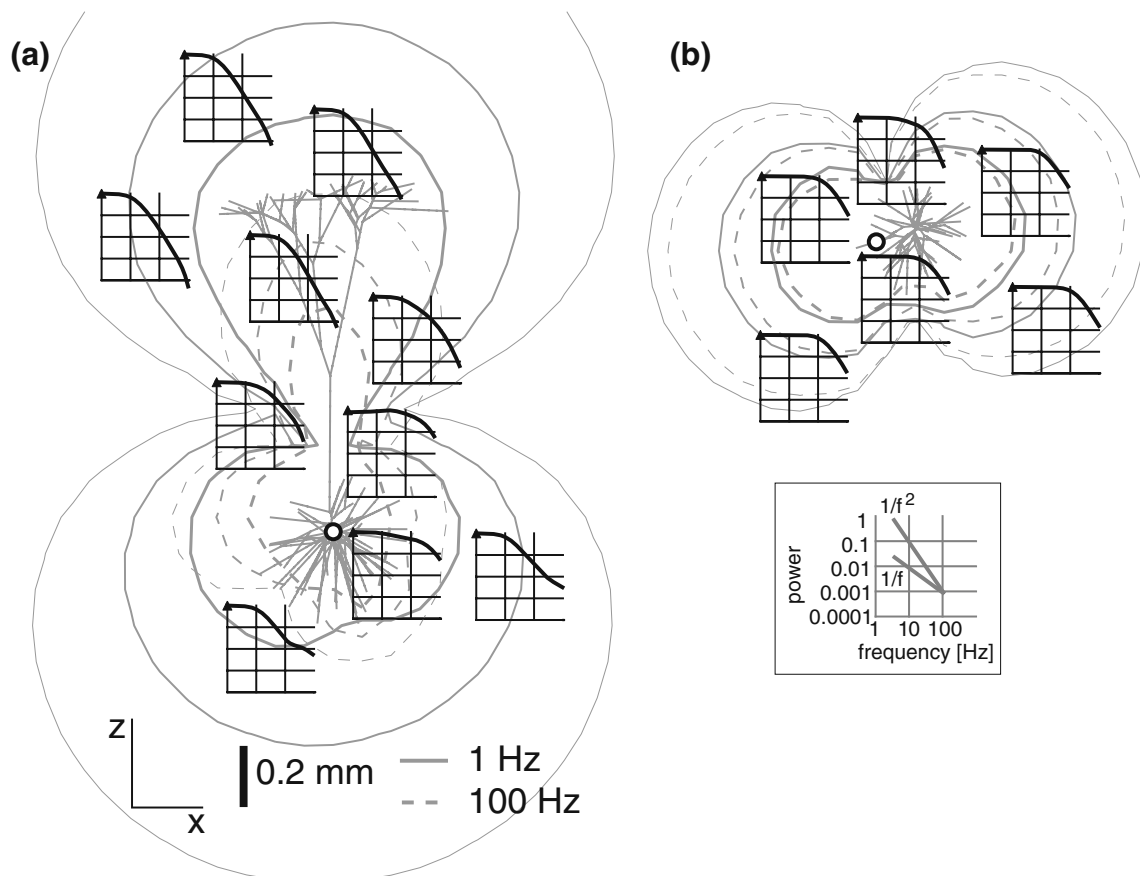


**Fig. 3** Calculated power spectra of local field potentials (LFPs) following injection of white-noise current into (a) the *soma* of the layer-5 pyramidal neuron considered in Fig. 2 and (b) a

dendritic synapse of the layer-4 stellate cell (cf. Fig. 1(c)). The current injection points are marked with circles. See caption of Fig. 2 for detailed explanation of the plots

situation. But the change compared to the results in Fig. 2(a) based on the default value of  $R_m$ , is less compared to decreasing the value of  $R_m$  by a factor of ten, cf. Fig. 4(a). This illustrates the fact that a change of the membrane resistance not only changes the membrane time constant, but also the frequency-dependent length constant of the current dipole (cf. Eqs. 10–11 in Pettersen and Einevoll 2008). The overall change of the LFP spectra will thus depend on the detailed interplay between these variables and morphological quantities of the neuron and thus not follow a simple scaling rule suggested by considering changes in the membrane time constant alone.

The other key passive parameter is the specific axial resistance  $R_a$ , and in Fig. 4(c) and (d) we correspondingly show how the power spectra are altered when this parameter is reduced (Fig. 4(c)) or increased (Fig. 4(d)) by a factor ten, respectively, compared to the default value  $R_a=150 \Omega \text{ cm}$  used in Fig. 2(a). In Fig. 4(c) where  $R_a$  is reduced by a factor ten, we see that the 100-Hz equipotential contour lines resemble the 1-Hz contour lines much more than for the results for the default value of

$R_a$  in Fig. 2(a). This can be qualitatively understood on the basis of the length constant of the current dipole for an infinite cable which is proportional to  $1/\sqrt{R_a}$  (Koch 1998; Pettersen and Einevoll 2008). A reduced axial resistance implies a longer length constant, which in turn implies that the neuronal dendrites become electrically more compact. In analogy with the small low-pass filtering effect observed for frequencies below 100 Hz for the short-stick stellate neuron in Fig. 3(b), we see in Fig. 4(c) that the low-pass filtering cut-off in general is shifted to higher frequencies compared to the results for the default parameters in Fig. 2(a). This general shift of salient spectral features towards higher frequencies is also seen in the ‘band-pass’ spectra outside the stalk of the apical dendrite. Here the band-pass peak is shifted upwards by almost an order of magnitude compared to the result for the default value of  $R_a$  shown in Fig. 2(a). The opposite effect is observed in Fig. 4(d) where the specific axial resistance  $R_a$  is increased by a factor ten: since the length constant is reduced, the neurons will be electrically less compact and the typical low-pass cut-off frequencies reduced.

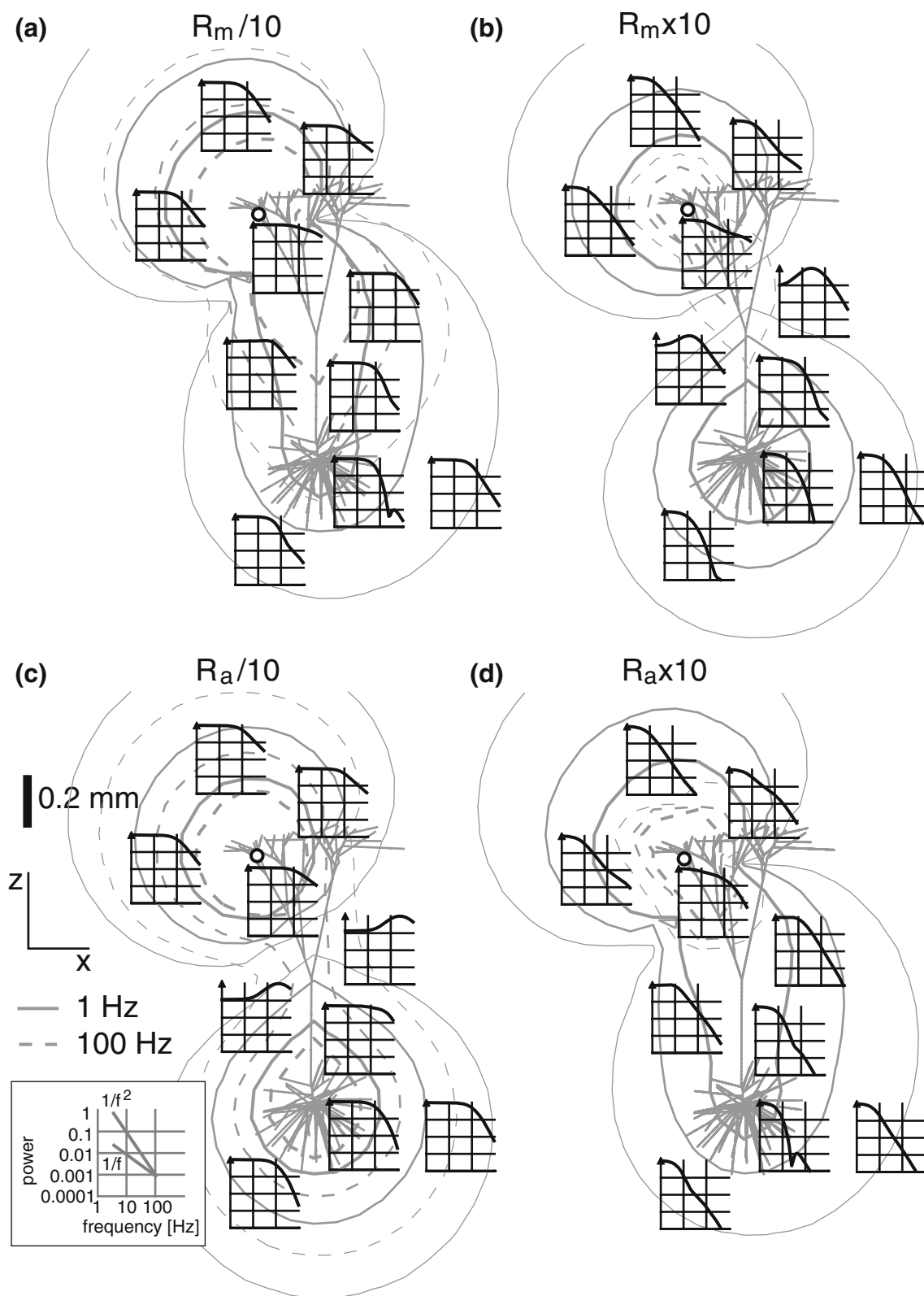


**Fig. 4** Calculated power spectra of local field potentials (LFPs) for the same situation as in Fig. 2(a), but different passive neuron parameters. **(a)** As in Fig. 2, but with specific membrane resistance reduced by a factor ten to  $R_m=3 \text{ k}\Omega \text{ cm}^2$ . **(b)** As in Fig. 2, but with specific membrane resistance increased by a factor

ten to  $R_m=300 \text{ k}\Omega \text{ cm}^2$ . **(c)** As in Fig. 2, but with specific axial resistance reduced by a factor ten to  $R_a=15 \text{ }\Omega \text{ cm}$ . **(d)** As in Fig. 2, but with specific axial resistance increased by a factor ten to  $R_a=1,500 \text{ }\Omega \text{ cm}$ . See caption of Fig. 2 for detailed explanation of the plots

### 3.4 Frequency dependence of membrane-current distribution

The previous subsections demonstrated the ubiquity of an intrinsic dendritic low-pass filtering effect of the LFP. They also demonstrated that the power spectra

vary strongly with recording position, and that the details of the spectra are determined by an interplay between neuronal morphology, synaptic input position and passive cable parameters. Figure 2 also illustrated the salient role of the transmembrane return currents in determining the characteristics of LFPs. In Fig. 5 we

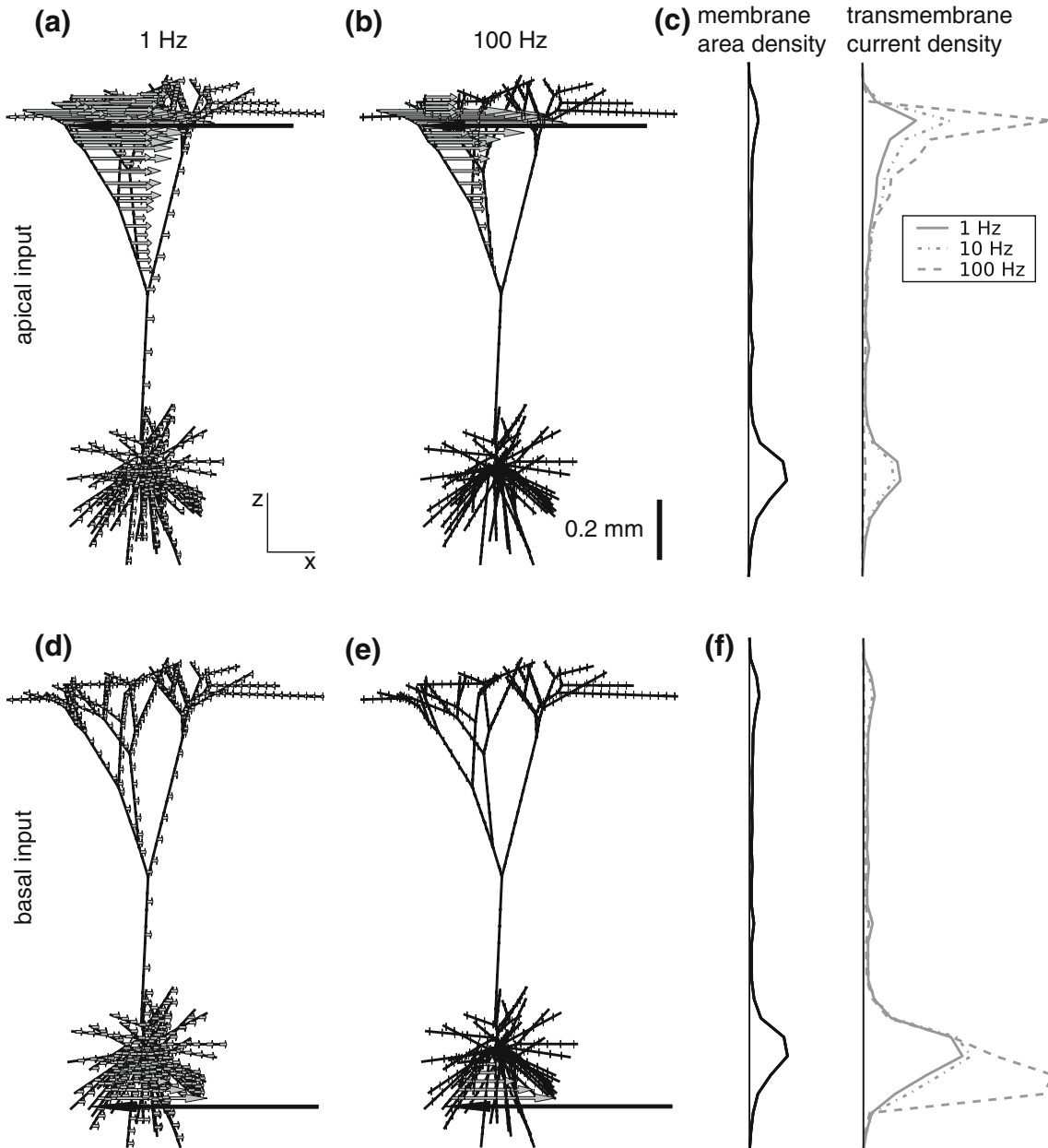


**Fig. 5** Illustration of frequency dependence of distribution of transmembrane currents following sinusoidal current injection into apical (*upper row*) or basal (*lower row*) synapse (*thick arrow in neuron figures*). The length of the rightward oriented arrows in the neuron figures in panels (a), (b), (d), and (e) represents the amplitude of transmembrane return currents following injection of currents at apical (a, b) and basal (d, e) positions, see thick leftward oriented arrow. The depth distributions of the transmembrane return currents for 1 Hz (*solid*), 10 Hz (*dash-dotted*),

and 100 Hz (*dashed*) are shown in panels (c) and (f) for apical and basal excitation, respectively. Note that the lengths of the arrows representing the return currents are normalized to have the same maximum return current in panels (a), (b), (d) and (e). In reality the amplitude of maximum transmembrane return currents is much larger for 100 Hz than for 1 Hz, see panels (c) and (f). The depth distribution of the total membrane area is also shown in panels (c) and (f)

illustrate further the core physical effect underlying this observed intrinsic dendritic low-pass filtering. In panel (a) the spatial distribution of transmembrane return currents (rightward arrows) following injection of a sinusoidal input current (1 Hz) in the apical dendrite (single thick leftward-oriented arrow) is shown. The length of the return-current arrows illustrates the amplitude of the corresponding sinusoidal return currents. As seen in panel (a) a substantial part of the apically injected current returns through the soma and basal dendrites. The corresponding return-current pattern for a 100 Hz sinusoidal current is shown in panel (b). Here, essentially none of the injected current returns through the basal region, all of it returns through the apical dendrites.

The effect is more clearly quantified by the curves in the panel (c) in Fig. 5, showing the depth distribution of total return current along the vertical extension of the pyramidal neuron. For the 1-Hz situation almost half of the return current leaves through the basal region where the depth distribution essentially follows the depth distribution of the total membrane area, see panel Fig. 5(c). For the 100-Hz case, on the other hand, almost all return current leaves through the apical dendrites. For 10 Hz an intermediate situation is observed.

In terms of generation of LFP both the 1-Hz and the 100-Hz situations depicted in Fig. 5(a)–(b) correspond to ‘open-field’ situations; see, e.g., Johnston and Wu (1995): the weighted mean position of the return currents is for both frequencies spatially displaced from the current injection point. However, the spatial distance between the current injection point and the mean position at which it returns to the extracellular medium, i.e., the *current dipole length* (Pettersen and Einevoll 2008), is very different in the two cases. For 1 Hz this dipole length is about half the distance between the current injection point and the soma, while for 100 Hz it is reduced to less than one tenth of this distance. The current dipole *strength*, which essentially corresponds to the absolute value of the current dipole *moment* described in Eqs. (4)–(6), is determined by the injected current multiplied by these current dipole lengths. Consequently, the dipole strength will be much larger for the 1-Hz situation than for the 100-Hz situation. At positions some distance away from the neuron, the LFP can be expected to be approximately proportional to this current dipole strength (Pettersen and Einevoll 2008). On these grounds the large reduction of the LFP in the 100-Hz situation compared to the 1-Hz situation seen in the power spectra of Fig. 2, is thus not unexpected.

The above example with apical synaptic inputs onto a large pyramidal neuron is the textbook example of an

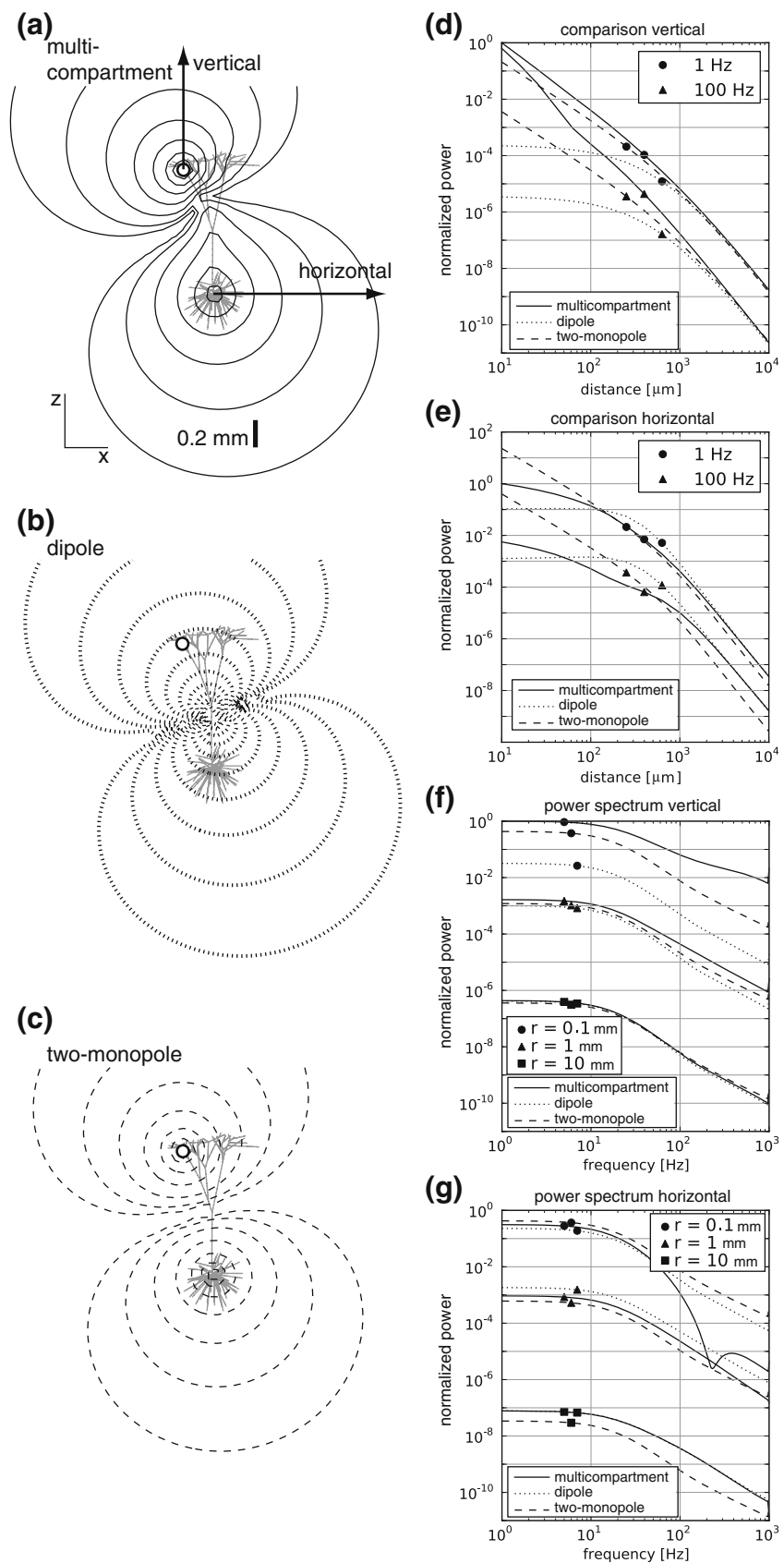
‘open-field’ situation which may generate large extracellular potentials (Johnston and Wu 1995). However, as seen in the panels (d–f) in Fig. 5, also a synaptic input onto a basal dendrite provide a current dipole. As seen in panels (d) and (f) a sizable fraction of the return current crosses the membrane in the apical dendrites for a 1 Hz sinusoidal current injected into the soma. For a 100 Hz injection current, however, essentially all of the return current leaves at the basal part of the neuron, cf. panels (e) and (f) in Fig. 5.

### 3.5 Current multipole approximations for LFP generation

In Pettersen and Einevoll (2008) it was found that the extracellular potential signature of action potentials could be well understood qualitatively, and to some extent also quantitatively, on the basis of frequency-dependent current dipoles accounting for the gross features of the spatial pattern of transmembrane currents. For action potential signatures the dominant frequencies are typically a few hundred hertz. For such high frequencies the relevant current dipole lengths are expected to be governed by the electrical cable properties of the dendrites protruding from the soma (Pettersen and Einevoll 2008). For the lower frequencies dominating the LFP, the current dipole length will to a larger extent be governed by the spatial extension of the entire dendritic structure. In Fig. 5, for example, we see for the apical-excitation case that roughly half of the injected synaptic current returns through the basal region, while the other half returns around the synapse. This implies that the current dipole length will be about half the vertical distance between soma and synapse.

Multipole expansions, where the electrical potentials are built up as sums over contributions from the various multipole terms (monopole, dipole, quadrupole, ...), have a long tradition in electrostatics (Plonsey 1969; Jackson 1998). Lately, this approach has also been used to investigate the origin of the extracellular potential signatures of action potentials (Pettersen and Einevoll 2008; Milstein and Koch 2008). In the present section we will pursue a similar approach and investigate to what extent simplified multipole expressions can account for the results based on our comprehensive multicompartment forward-modeling scheme. In panel (a) of Fig. 6 we show the LFP-power contour plot resulting from our multicompartment modeling scheme for the situation where a 1 Hz sinusoidal current is injected into a particular apical synapse (marked with an open dot). This comprehensive multicompartment line-source scheme will provide the ‘gold-standard’

**Fig. 6** Illustration of various multipole (*dipole*, *two-monopole*) approximations for LFP modeling. **(a)** Contour plot illustrating the variation of the 1-Hz power, i.e., square of Fourier amplitude, of the LFP with distance from neuron following sinusoidal current injection into an apical synapse (*circle*). Full multicompartment forward-modeling scheme is used, i.e., Eq. (1). The arrows illustrate the ‘vertical’ and ‘horizontal’ directions considered in detail in panels **(d)–(g)**. **(b)** Same as **(a)** for *dipole approximation*, i.e., Eq. (8). **(c)** Same as **(a)** for *two-monopole approximation*, i.e., Eq. (10). **(d)** LFP power along the ‘vertical’ direction (see panel **(a)**) for multicompartment, dipole, and two-monopole modeling schemes, respectively. Distance is measured relative to apical synapse (*circle*). Results for 1 Hz and 100 Hz sinusoidal current injections are shown, normalized to the multicompartment value for 1 Hz. **(e)** Same as **(d)** for the ‘horizontal’ direction as measured out from soma. Results are normalized to the multicompartment value for 1 Hz. **(f)** Frequency dependence of the LFP power for three particular distances from the neuron (0.1 mm, 1 mm, 10 mm) in the ‘vertical’ direction. The spectra are normalized so that the LFP power for the multicompartment model for 1 Hz at the distance 10  $\mu\text{m}$  is unity. **(g)** Same as **(f)** for the ‘horizontal’ direction. Note that also here the spectra are normalized so that the multicompartment LFP power for 1 Hz at the distance 10  $\mu\text{m}$  in the ‘vertical’ direction is unity



results against which our multipole approximations will be compared.

Due to current conservation there will be no current *monopole* contribution to the LFP, and the first non-zero contribution will in general come from current *dipoles*. In the far-field limit, i.e., when the distance  $r$  to the current dipole is much larger than the current dipole length, the dipole LFP expression is given by (Pettersen and Einevoll 2008):

$$\phi_d(\mathbf{r}, t) = \frac{1}{4\pi\sigma} \frac{|\mathbf{p}(t)| \cos\theta}{r^2} . \tag{8}$$

Here  $\mathbf{p}(t)$  is a *current dipole moment* which in general is given by

$$\mathbf{p}(t) = p_x(t) \mathbf{e}_x + p_y(t) \mathbf{e}_y + p_z(t) \mathbf{e}_z \tag{9}$$

where  $p_x(t)$ ,  $p_y(t)$ , and  $p_z(t)$  are defined in Eq. (4). Further,  $\theta$  is the polar angle relative to the dipole axis and  $r$  the radial distance to the dipole position (see, e.g., Fig 2(a) in Pettersen and Einevoll (2008) for an illustration). With a sinusoidal input current it follows from the linearity of the model that the individual components, i.e.,  $p_x(t)$ ,  $p_y(t)$ ,  $p_z(t)$ , also will vary sinusoidally in time, cf. Eq. (5). In general the phases of the different components ( $\gamma_{fx}$ ,  $\gamma_{fy}$ ,  $\gamma_{fz}$ ) in Eq. (5) will be different, and the system will then not reduce to a dipole oriented along a particular fixed spatial direction. In the present application, however, we do the approximation of assuming identical phases, i.e.,  $\gamma_{fx} = \gamma_{fy} = \gamma_{fz} = \gamma_f$ . We then obtain a sinusoidally oscillating dipole along a *fixed axis* with an oscillatory current dipole moment given by  $\mathbf{p}_{fa}(t) = \mathbf{p}_0(f) \sin(2\pi ft + \gamma)$ , cf. Eq. (6).

In panel (b) of Fig. 6 we show the LFP-power contour plots assuming this *dipole approximation*. This plot is found by applying  $\mathbf{p}_{fa}$  from Eq. (6) in the dipole expression in Eq. (8) to get the LFP signal. For this plot the current dipole has been placed in the ‘middle’ of the neuron, i.e., straight above the soma at a height corresponding to halfway between the lowest and uppermost points of the dendritic structure. A visual comparison of the dipole-approximation results with the corresponding multicompartment results in panel (a) reveals a very good agreement at distances far away from the neuron. Close to the neuron the agreement is as expected poor.

An obvious question to ask is how far away from the neuron one has to be in order for the dipole-approximation to work. As illustrated by panels (d) and (e) in Fig. 6, this depends on direction. Here we focus on two directions: (1) vertically up from the position of the apical input current (labeled ‘vertical’, cf. panel (a)), and (2) horizontally out from the soma (labeled ‘horizontal’, cf. panel (a)). The resulting LFP power for the ‘vertical’ direction is shown in panel (d). For

the 1-Hz situation depicted in panels (a) and (b) we see that the dipole approximation (dotted line) gives predictions in excellent agreement with the multicompartment model (solid line) for distances larger than about 1 mm. In panel (d) we also show the corresponding comparison when the input current is oscillating at 100 Hz. Also here we observe agreement at distances larger than about a millimeter or two. The same comparison for the ‘horizontal’ direction is shown in panel (e), and the same excellent agreement is observed in the far-field limit. However, the transition to the far-field regime appears to occur for slightly larger distances than in the ‘vertical’ direction.

The results in panels (d) and (e) of Fig. 6 clearly demonstrate the expected inadequacy of the far-field dipole approximation (Eq. 8) for positions close to the neuron. The contour plot for the multicompartment model in panel (a) shows that the 1-Hz LFP power peaks both around the synaptic-input position and the soma, in accordance with the observation of the plots of the transmembrane currents in Fig. 5. This suggests an alternative *two-monopole* approximation  $\phi_{tm}(\mathbf{r}, t)$  for the LFP,

$$\phi_{tm}(\mathbf{r}, t) = \frac{I_{tm}(t)}{4\pi\sigma} \left( \frac{1}{|\mathbf{r} - \mathbf{r}_{syn}|} - \frac{1}{|\mathbf{r} - \mathbf{r}_{soma}|} \right) , \tag{10}$$

where the current is assumed to enter or exit the neuron only at two positions: the synapse and the soma. From current conservation it follows that the current  $I_{tm}(t)$  entering the neuron at the apical synapse ( $\mathbf{r}_{syn}$ ) must leave at the soma ( $\mathbf{r}_{soma}$ ). In this two-monopole approximation the current  $I_{tm}(t)$  does *not* correspond to the true synaptic input current. Rather,  $I_{tm}(t)$  is set to give the correct magnitude of the current dipole moment, i.e.,

$$I_{tm}(t) \equiv |\mathbf{p}_{fa}(t)|/\lambda_{tm} . \tag{11}$$

Here  $\lambda_{tm} \equiv |\mathbf{r}_{syn} - \mathbf{r}_{soma}|$ , i.e., the distance between the synapse and soma. Since the *direction* of the current dipole moment  $\mathbf{p}_{fa}(t)$  in general will not exactly coincide with the direction from synapse to soma, the two-monopole approximation will not converge to the dipole approximation in the far-field limit. However, with this choice of  $I_{tm}(t)$  one may still hope to obtain reasonably correct predictions for the LFP also for large distances.

In panel (c) of Fig. 6 we show the LFP-power contour plot for the 1-Hz situation assuming this *two-monopole approximation*, i.e., Eq. (10) with (the sinusoidally varying)  $I_{tm}(t)$  given by Eq. (11). A visual comparison of the contour plots for the two-monopole approximation with the corresponding multicompartment plots in

panel (a) reveals qualitatively similar spatial patterns. And indeed, in panel (d) the two-monopole approximation is seen to follow the multicompartment results closely when one moves along the ‘vertical’ direction depicted in panel (a). The agreement is particularly good for current modulations of 1 Hz, but also for 100 Hz the two-monopole approximation is seen to give reasonable results for distances larger than a few hundred micrometers.

As seen in panel (e) of Fig. 6 the performance of the two-monopole model in the ‘horizontal’ direction is much poorer. For one, this model significantly deviates from the multicompartment results also for the largest distances. This error stems from the deviation between the direction of the true current dipole moment and the line between the apical synapse and the soma. This deviation can also be seen directly by close inspection of the contour plots in panels (a–c): the lines (in these 2D plots) corresponding to zero LFP power have slightly different directions for the dipole and two-monopole approximations. This ‘direction error’ of course also affects the LFP predictions in the ‘vertical’ direction, but much less so.

Secondly, the two-monopole approximation predicts much too large LFP power close to the soma, i.e., for distances smaller than about 100 micrometers in the ‘horizontal’ direction. Such short distances corresponds to positions well inside the bush of basal dendrites, and as seen in panels (a) and (b) in Fig. 5, the transmembrane currents in the basal region appear to be spread out all over the basal dendrites, rather than focused in the soma. The point-like monopolar expression in Eq. (10) representing the contribution from the transmembrane currents in the soma region thus clearly provides a poor approximation, as demonstrated quantitatively by the curves in Fig. 6(e).

Further, while the soma region provides the dominant contribution to the return current for the 1-Hz situation as illustrated, e.g., by the LFP power contour plots Fig. 2(a) and by the plot of the transmembrane currents in Fig. 5(a), this is not generally the case for higher frequencies. The corresponding results for the 100-Hz situation in Figs. 2(a) and 5(a) reveal that the return currents are strongly shifted in the direction of the apical synapse so that the ‘center-of-gravity’ of the return current is far above the soma. This explains the even larger overestimation of the LFP power by the two-monopole models seen in Fig. 6(e) for 100 Hz compared to 1 Hz, for horizontal distances from the soma less than a few hundred micrometers.

Finally, in panels (f) and (g) of Fig. 6 we investigate the power spectra due to the intrinsic low-pass filtering effect at three different distances (0.1 mm, 1 mm,

10 mm) along both ‘vertical’ and ‘horizontal’ directions. At all positions we observe sizable low-pass filtering effects for frequencies above about 10 Hz. The exact functional form of the dampening of high frequencies vary, but for the largest distances (1 mm, 10 mm) a decay of the LFP power approximately following  $1/f^2$  relationships are commonly seen for frequencies above 50 Hz. For the largest distance (10 mm) the dipole approximation is seen to predict the filtering characteristics excellently. For the two-monopole approximation the success is more mixed: it works well in the ‘vertical’ direction, but poorly in the ‘horizontal’ direction. For the intermediate distance (1 mm) the success of both approximations is more limited, and for the shortest distance considered (0.1 mm) they essentially fail. For example, in the ‘horizontal’ direction a sharp dip in the amplitude spectrum is observed for frequencies around 200 Hz in the full multicompartment model. This effect is likely due to details of the basal dendritic structure providing subtle cancelation effects at these frequencies. Such a phenomenon can clearly not be accounted for by our two approximate models where the detailed dendritic structure has been neglected. Further, in the ‘vertical’ direction the full multicompartment model predicts a power-law behaviour close to  $1/f$  over a wide frequency range for this shortest distance (0.1 mm). This contrasts the predicted power laws for the two approximate schemes which have much steeper frequency decays.

### 3.6 Current dipole approximation for LFP

In the previous section we focused on the special case where the synaptic current was provided by a single apical synapse. For this special case we found that the *dipole* approximation in Eq. (8), combined with the approximate current dipole moment  $\mathbf{p}_{fa}(t)$  given by Eq. (6), predicted the LFP power accurately at sufficiently large distances from the neuron, cf. Fig. 6. With the proper incorporation of *frequency-dependent* current dipole moments, the dipole approximation also appeared to explain main features of the observed high-frequency dampening in this far-field limit.

In the present section we investigate to what extent this LFP dipole approximation also applies for synapses positioned on other parts of the dendritic tree. In panel (a) of Fig. 7 we first illustrate the magnitude and direction of the current dipole moments for synapses at a few selected places on the dendritic tree. Sinusoidal input current at three different frequencies, 1 Hz, 10 Hz, and 100 Hz, are considered. The figures illustrate several qualitative points: (1) the current dipole moments are typically roughly directed along a straight line

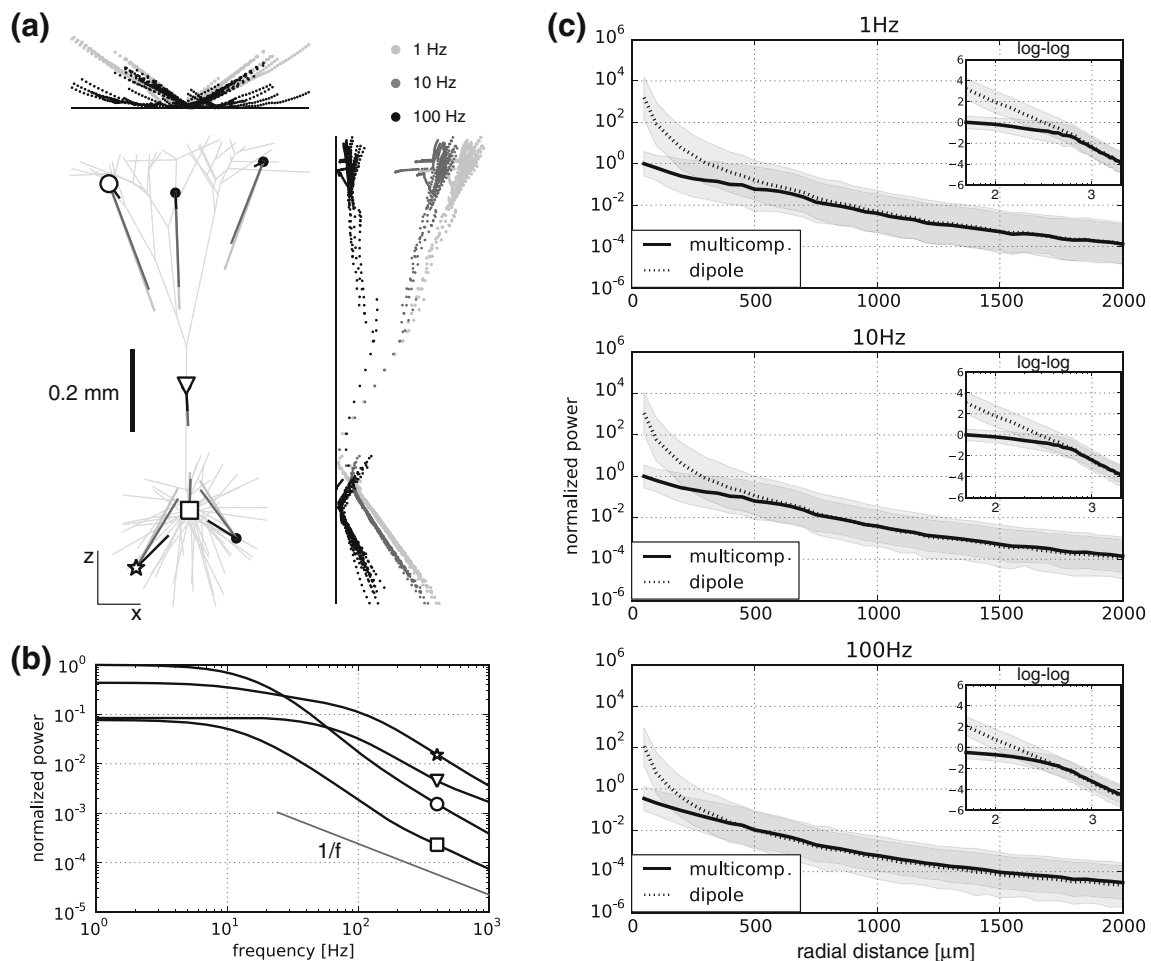


**Fig. 7** Current dipole moments and the LFP dipole approximation for various synaptic positions. **(a)** Illustration of direction and amplitudes of current dipole moments  $\mathbf{p}_0$  (cf. Eq. (7)) for a set of synaptic positions (black dots) superimposed on the dendritic structure. The figure shows the projection of these dipole moments into the 2D plane of the figure for the 1-Hz, 10-Hz, and 100-Hz situations. Lengths of line segments are proportional to current dipole-moment amplitudes. Dot plots on the right illustrates the magnitude of the vertical component  $p_{0z}$ , cf. Eq. (5), versus the vertical position of the synapse for the full number of synapses (1,072; one for each compartment in the multicompartment model). Dot plots above correspondingly illustrate the magnitude of the horizontal component  $p_{0x}$  for the same group of synapses (for the 1-Hz and 100-Hz situations, only). Color code: 1 Hz sinusoidal synaptic current: light grey, 10 Hz: darker grey, 100 Hz: black. **(b)** Illustration of frequency dependence of power of current dipole moments, i.e., square of Fourier amplitudes  $\mathbf{p}_0(f)$  defined by Eq. (6), for four different synaptic positions marked in **(a)** distal apical dendrite (circle), main apical dendrite (triangle), soma (square), basal dendrite (star). The same synaptic current is injected for all four situations, and the results have been normalized to the power of the current dipole moment for the distal apical-dendrite case for 1 Hz. **(c)** Illustration of accuracy of LFP dipole approximation for full group of 1,072 synaptic input positions considered in **(a)**. Mean values of logarithms of LFP values from full multicompart

ment  $\phi$  (Eq. (1)) are illustrated by solid lines. Surrounding grey bands above and below these lines correspond to the LFP values within the standard deviation (of the logarithm of LFP) around the mean. Results are shown as a function of radial distance from the ‘mid-point’ of the neuron (i.e., straight above the soma at a height corresponding to halfway between the lowest and uppermost points of the dendritic structure). For each radial distance  $r$  the LFP is evaluated separately for the 1,072 synaptic positions considered. Further, for each of these synaptic positions the LFP is calculated at a randomly selected spatial point with the constraint that the vertical position, i.e.,  $z$ -value, does not go above or below the vertical extension of the neuron. The mean value at each radial distance corresponds to the mean of the logarithm of these 1,072 calculated LFP values. Likewise, the standard deviation at each radial distance corresponds to the standard deviation of the logarithm of these 1,072 calculated LFP values. The dashed lines, with the surrounding grey bands, correspondingly illustrate the mean and standard deviation of the dipole-approximation values  $\phi_d$  (Eq. (8)) found by using the same averaging procedure. The current dipole is placed in the ‘mid-point’ of the neuron as it is described above. The inset figures show the same results with double-logarithmic axes ( $\log_{10}$ ). All results are normalized to the value of the LFP power found at the smallest distance considered (50  $\mu\text{m}$ ) for the 1-Hz situation in the full multicompart

connecting the synaptic input position and the soma, and (2) the magnitude of the current dipole moments is reduced from 1 Hz to 10 Hz, and even more so from 10 Hz and 100 Hz. Thus also the current dipole moment exhibits a prominent intrinsic low-pass filtering effect.

Above and to the right of the neuron shown in Fig. 7(a) a large collection of magnitudes of the horizontal ( $p_{0x}$ , cf. Eq. (5)) and vertical ( $p_{0z}$ ) components of the current dipole moment are depicted. Each point corresponds to a synapse placed in one of the 1,072 compartments representing the neuron in the multicompartment calculation scheme. The horizontal and vertical current dipole components are plotted as functions of the horizontal and vertical positions of the synapses, respectively. For the vertical component ( $p_{0z}$ ) a main salient feature is immediately apparent: for 1 Hz the magnitude of the current dipole moment is roughly proportional to the distance from the soma region. This applies for synapses both above and below the soma. A closer inspection of the figure reveals that for the 1-Hz input the ‘center-of-mass’-position, i.e., the synaptic position for which a current input gives no current dipole moment, is more than 0.1 mm above the soma on the thick apical dendrite. Thus also a synaptic current injected into the soma will give a sizable current dipole moment, and consequently also a sizable LFP, cf. Fig. 1(b).

The lack of generation of a current dipole moment does in any case not mean that no LFP will be generated since higher order multipole moments will not be zero. For example, injection of current at the synaptic position about 0.1 mm above the soma resulting in a negligible current dipole moment, gives a sizable current quadrupole moment. We confirmed this by direct numerical evaluations of an LFP power contour plot for this situation which indeed revealed a ‘clover-like’ spatial pattern characteristic for quadrupoles (results not shown).

The rough proportionality of the vertical component of the current dipole moment with distance from soma seen for the 1-Hz situation in Fig. 7(a), suggests that the current dipole qualitatively can be pictured as a fixed amount of *net* current entering in the synapse region, i.e., the synaptic input current minus the return current in the vicinity of the synapse, with the same net current leaving from the soma region. Then the vertical component of the dipole moment will be roughly proportional to the vertical distance between synapse and soma, in correspondence with what is observed in Fig. 7(a).

Qualitatively similar results are observed for the current dipole moment in the 10-Hz situation. The magnitude of the dipole moments are generally somewhat smaller than for 1 Hz, reflecting that the net current

propagating from the synapse to the soma, thus setting up the current dipole, is reduced due to the electrical cable properties of the dendritic structure. For 100 Hz a quite different picture is seen. Here a very small vertical component of the current dipole moment is seen for apical synapses, reflecting that most of the injected current return to the extracellular medium in the apical region, cf. Fig. 5(b). The distribution of the magnitudes of the horizontal components  $p_{0x}$ , shown above the depicted neuron in Fig. 7(a), is less characteristic. But also here the 100 Hz dipole components are generally seen to be much smaller than the 1 Hz dipole components.

In Fig. 7(b) we illustrate the frequency dependence of the dipole moments further. Here we show the power of the dipole moments, i.e.,  $|\mathbf{p}_0(f)|^2$  where  $\mathbf{p}_0(f)$  is defined by Eq. (6), for frequencies between 1 and 1,000 Hz, generated by injecting currents at four different synaptic positions. Prominent low-pass filtering effects are observed for all situations, but the detailed form of the power spectra vary. The strongest low-pass filtering is seen for inputs at the apical synapse (marked with a circle in panel (a)) and in the soma (square in panel (a)). The low-pass filtering effect is weaker and shifted to higher frequencies for inputs on the main apical dendrite (triangle in panel (a)) and on the basal dendrite (star in panel (a)). This further illustrates that the low-pass filtering effect seen in power spectra of extracellular potentials not only depends on the position of the recording electrode, but also on the distribution of the synaptic inputs generating the potentials.

Calculated current dipole moments, such as the ones depicted in Fig. 7(a), can now be used to calculate the LFP at various spatial positions using the dipolar expression in Eq. (8). In panel (c) we compare results for the LFP power calculated by this dipolar expression against the results from the full multicompartment model for our three different frequencies (1 Hz, 10 Hz, 100 Hz). The panels compare, as a function of radial distance, the mean and the spread of the logarithms of the LFP power calculated using the dipole-approximation with the corresponding values found from using the full multicompartment scheme. These statistical measures are found by averaging over results from injecting current at the 1,072 different synaptic positions considered, see caption of Fig. 7 for details.

For the largest distances ( $\sim 1\text{--}2$  mm) considered in the plots in Fig. 7(c), one is approaching the far-field regime, and the dipole approximation can be expected to be fairly precise. This is indeed observed in the plots. The averages of the observed dipolar LFP power are seen to approach the multicompartment LFP power for the largest distances for all three frequencies consid-

ered (1 Hz, 10 Hz, 100 Hz). As illustrated by the inset figures showing the same results in double-logarithmic plots, the multicompartment results for the LFP power indeed decay as  $1/r^4$ , characteristic for a current dipole, for radial distances above  $\sim 1$  mm. Interestingly, the far-field limit appears to be reached faster, i.e., for smaller radial distances, in the 100-Hz situation than in the 1-Hz situation. This can be understood on the basis of the shorter effective current-dipole length for the 100-Hz situation seen in Fig. 7(a): since the transition to the far-field regime depends on the ratio between the current-dipole length and the radial distance, a shorter current dipole length implies an earlier transition to the far-field regime when moving away from the neuron.

For the smallest radial distances considered ( $< 0.5$  mm), we observe as expected that the dipole approximation generally does a poor job of predicting the LFP power. As seen for all three frequencies considered in Fig. 7(c), the dipole approximation following a  $1/r^4$  dependence, tends to overestimate the LFP in this regime. Note that in panels (d–e) in Fig. 6 it was found that the dipole approximation instead underestimated the true LFP for the shortest distances. The difference is simply due to the different origin and directions of the axes considered, i.e., distance along the ‘vertical’ and ‘horizontal’ directions starting in the apical synapse and the soma, respectively, in panels (d–e) in Fig. 6 versus the radial distance measured from the dipole position at the middle of the neuron in Fig. 7(c).

## 4 Discussion

### 4.1 Intrinsic dendritic low-pass filtering effect

The origin of the observed frequency spectra of EEG and extracellularly recorded potentials in the brain (LFP) has attracted considerable interest (Pritchard 1992; Beggs and Plenz 2003; Bedard et al. 2004, 2006a, b; Buzsaki 2006; Pettersen and Einevoll 2008; Bedard and Destexhe 2009; Miller et al. 2009; Milstein et al. 2009). We previously showed that there is an unavoidable low-pass frequency-filtering effect of the extracellular action-potential signature due to the electrical cable properties of the neuronal dendrites (Pettersen and Einevoll 2008). In action potentials the dominant frequencies are typically a few hundred hertz, but a main finding in the present paper is that the same intrinsic dendritic filtering effect also pertains to the lower frequencies dominating in typical LFP and EEG spectra, and is particularly prominent for large layer-5 pyramidal neurons. Our model results have demon-

strated an omnipresent low-pass filtering effect on the LFP spectra following synaptic activation. For our example pyramidal neuron we generally observed sizable filtering effects for frequencies above  $\sim 10$  Hz. The magnitude and form of this filtering effect will naturally depend on, e.g., the morphology of the dendritic structure and spatial distribution of activated synapses of the neuron in question. However, all neurons will to some degree exhibit such filtering of their contributions to the overall LFP, and any theory aspiring to explain the physical origin of measured LFP or EEG spectra must therefore also consider this intrinsic dendritic filtering effect.

In an important study Bedard et al. (2006b) attempted to model observed LFP power spectra on the basis of simultaneously recorded spiking activity spectra. They concluded that a factor  $1/f$  was ‘missing’ to account for the observed LFP power spectra for frequencies less than  $\sim 70$  Hz, and they suggested that this missing factor could be due to frequency attenuation in the extracellular medium itself. The present study suggests as an alternative, or maybe supplementary, explanation that the intrinsic dendritic-filtering effect may contribute to a missing factor  $1/f$  in their model for LFP power spectra. For the present large pyramidal neuron the LFP signal is expected to be dominated by contributions from neurons less than about 0.5 mm away (Lindén et al. 2009a). For the ‘vertical direction’ in Fig. 6(f) we found that the LFP power spectra for the shortest distance considered (0.1 mm) indeed are in qualitative accordance with a  $1/f$  decay, at least between 10 Hz and 100 Hz. In the ‘horizontal’ direction in Fig. 6(g), however, a steeper decay with frequency was observed for this short distance (0.1 mm), but this observation may have been confounded by an observed resonance phenomenon around 200 Hz for this particular modeling example. In any case, the conclusion from our study is not the prediction of a particular power-law behaviour for the LFP, rather that the intrinsic dendritic filtering effect must be included when attempting to model such spectra. Experimental LFPs stem from a sum of numerous contributions from a population of neurons in the vicinity of the recording electrode (Liu and Newsome 2006; Berens et al. 2008; Katzner et al. 2009; Xing et al. 2009). A more comprehensive numerical investigation of the LFPs generated by such populations of neurons is thus needed to draw firmer conclusions on this (Lindén et al. 2008, 2009a).

A striking observation in our study is that the recorded LFP signal from a single synaptic event varies dramatically with the recording position. The extracellular signature of a particular synaptic event will vary not only in magnitude and temporal shape, but

also in overall sign (cf. Fig. 1). Likewise, the form of the LFP power spectra will depend strongly on the recording position: a large variation in the typical low-pass cut-off frequencies is seen, and band-pass properties are even observed at some spatial locations. The experimental LFP observed will correspond to a weighted sum over contributions from many different types of neurons, located at different distances from the recording electrode, receiving numerous synaptic inputs targeting different parts of dendritic trees. As the dominant contributions to the sum providing the LFP cannot be expected to be independent of cortical area and depth, one cannot *a priori* expect common power laws for all observed LFP or EEG power spectra.

Our study revealed a systematic dependence of the intrinsic dendritic-filtering effect on the distance from the recording position to the synaptic input. In general, the high-frequency attenuation of the LFP will be less at positions close to the active synapse where the LFP gets large contributions from the synaptic input current itself. Farther away the LFP will get stronger contributions from the transmembrane *return* currents which in general will be low-pass filtered versions of the synaptic input current (due to the electrical cable properties of the dendrites). In the present paper this was most explicitly illustrated by the set of LFP power spectra in Figs. 2–4, but the effect is generic and also applies to, for example, extracellular action potential signatures (Pettersen and Einevoll 2008; Pettersen et al. 2010). This points to a way to infer the spatial distribution of active synapses acting on a neural population from recordings with linear (laminar) multielectrodes inserted perpendicularly on the cortical layers (Einevoll et al. 2007): the current source-density (CSD) profile informs about the vertical extension of an activated population of, say, layer-5 pyramidal neurons, but may not *per se* be able to distinguish the situations with *inhibitory* synapses acting in the basal dendritic region from *excitatory* synapses acting in the apical region. In both cases one will observe a sink-source dipole with the current sink in the apical region. However, the present results suggest that in the former case there will be more high-frequency components in the CSD at vertical positions inside the basal bush than at vertical positions at the level of the apical dendrites. In the latter case the situation will be reversed.

#### 4.2 Dipole and two-monopole approximations to the LFP

The use of current dipoles in the modeling of bioelectric signals, and in particular EEG signals, is not new

(Plonsey 1969; Freeman 1980; Nunez and Srinivasan 2006; Grech et al. 2008). In the application to EEG signals one has typically aimed to account for the observed signals in terms of contributions from a set of ‘mesoscopic’ current dipole sources, and the distances between the current dipoles and the EEG recording position have typically been assumed to be so large that the far-field dipole approximation apply (Nunez and Srinivasan 2006; Grech et al. 2008). Here we have focused on the fundamental microscopic dipoles underlying these mesoscopic dipole sources, namely the current dipoles set up by individual neurons (Murakami and Okada 2006; Pettersen and Einevoll 2008).

As in the analysis of the extracellular signature of action potentials (Pettersen and Einevoll 2008) we find the *current dipole moment* to be a crucial concept for gaining both qualitative and quantitative understanding of the relationship between the underlying activity in the neuron and the generated extracellular potentials. For the action-potential signature investigated in Pettersen and Einevoll (2008) this dipole moment was typically found to be determined by the electrical properties of the dendritic branches protruding out from the soma. Consequently the *current dipole length*, a measure of the distance between the soma and the average spatial position at which the return currents pass the dendritic membrane, was found to depend mainly on dendritic parameters such as diameter, capacitance, and axial and membrane resistances. In contrast, for the lowest frequencies considered in the present LFP spectra (<10 Hz), we found here that the main dendritic feature determining the current dipole length, and the current dipole moment, appeared to be the spatial distance between the active synapse and the soma (cf. Fig. 7(a)). At such low frequencies rough estimates of the direction and relative magnitude of the current dipole moments for various synaptic inputs can thus be obtained by anatomical considerations alone. However, in general the frequency-dependent current dipole moment (cf. Fig. 7(b)) will be determined by a combination of morphological and electrical membrane properties.

Used in combination with the well-known far-field dipole expression in Eq. (8), the current dipole moment was shown to predict the ‘true’ LFP (found in our comprehensive multicompartments scheme) accurately at large distances, i.e., a few millimeters away from the neuron. We also found that this dipole approximation could account for salient features of the intrinsic low-pass filtering effect, i.e., that the low-pass frequency filtering of the LFP could be traced back to low-pass frequency filtering of the current-dipole moment.

As expected we found this far-field approximation to break down close to the neuron, partially because it does not explicitly represent the two dominant contributions from the synapse and soma regions, respectively. We thus also investigated a *two-monopole* approximation, i.e., a 2-compartment model where all transmembrane current is assumed to enter the neuron at one point (the synapse) and leave at the other (the soma). Further, the transmembrane current was set to give the right *magnitude* of the current dipole moment. For our example in Fig. 6 we found the two-monopole approximation to give very good predictions in the vicinity of the active synapse, much better than the dipole approximation. However, for our example with excitation of an apical synapse, we found the two-monopole approximation to predict far too big LFPs for positions inside the bush of basal dendrites. There are likely two main reasons for this discrepancy: (1) For situations where the return current indeed is focused in the soma region (such as for low-frequency apical synaptic inputs onto the layer-5 example neuron), the true transmembrane current in the soma region is, due to the extensive basal dendritic structure, much more diffuse than what is implicitly assumed in the two-monopole model. (2) For high-frequency synaptic input the cable properties of the neuron will in general reduce the amount of return current leaving from the soma region, and the ‘center-of-gravity’ of the return current will be positioned closer to the position of the synaptic input, cf. Fig. 5. This will naturally violate the assumption inherent in the two-monopole approximation where the return monopole is set to be at the soma.

An alternative version of the two-monopole model would be to move the return-current monopole from the soma to the position of the center-of-gravity for the return current. This center-of-gravity position will depend on frequency, and such a two-monopole approximation would likely yield more accurate results than the present two-monopole model. However, the calculation of the center-of-gravity position will involve numerical solution of the full compartmental model to obtain all transmembrane currents, making the implementation of the approximation almost as cumbersome as using the comprehensive line-source scheme. A main advantage of the present two-monopole model is that the position of the two monopoles is determined solely by the neuronal morphology and thus easy to specify (even though specification of the magnitude of the monopole currents requires knowledge about the dipole-moment magnitude, which in turn must be calculated based on knowledge of all transmembrane currents).

#### 4.3 Network modeling of LFP, ECoG and EEG

A natural ambition of neural network modeling should be to predict not only spike trains, but also extracellular potentials. One approach for achieving this would be to simulate networks of multicompartmental neurons so that the generation of action potentials and the transmembrane currents needed to evaluate extracellular potentials, could be calculated simultaneously. However, spiking neural networks are more commonly modeled by means of 1-compartment neurons which by design do not generate an extracellular potential: a neuron model must have at least two compartments to generate an extracellular potential (Pettersen et al. 2010). In such cases ad hoc formulas relating synaptic currents to LFP have been used to provide LFP predictions from network simulations, see, e.g., Mazzoni et al. (2008).

The forward-modeling scheme offers a method for testing of such putative add-on formulas for predicting extracellular potentials. Our present work unfortunately does not suggest any such simplifying formula for prediction of LFPs recorded well inside the active cortical tissue. For the present pyramidal neuron we expect the LFP signal to get most of its contributions from neurons within a radius of less than 0.5 mm (Lindén et al. 2009a), an estimated spatial range of the LFP in qualitative accordance with recent experimental estimates (Katzner et al. 2009; Xing et al. 2009). As seen in Fig. 6 both the dipole approximation (Eq. 8) and the two-monopole approximation (Eq. 10) generally give inaccurate results of the LFP for such small distances. Simplifying formulas based on these approximations thus appears ruled out. This observation thus clearly questions the approach of interpreting intracortical LFP recordings in terms of contributions from dipolar sources (Church et al. 1985; Yvert et al. 2001).

The development of simplified schemes for predicting contributions to extracellular potentials recorded at the cortical surface (ECoG) is maybe more feasible. As seen in Fig. 6(d) the two-monopole approximation does fairly well, in particular for the 1-Hz situation, in the vertical direction for positions more than 0.1 mm or so above the apical synapse. This suggests that this two-monopole approximation may be useful for predicting ECoG signals. In fact a similar two-monopole approximation was suggested by Freeman (1980) to interpret ECoG signals recorded by electrode arrays placed on the brain surface. However, here we only explored the two-monopole approximation for the situation with an apical synapse where the LFP recorded immediately above is dominated by a rather focal sink. Even in this situation, the agreement with the correct

multicompartmental results was not more than fair. With other synaptic inputs which generate more diffuse patterns for transmembrane currents in the apical dendritic tree, a lesser performance of the two-monopole approximation must be expected. A more comprehensive investigation also considering morphologies of other neuron types expected to give large contributions to the ECoG signal (e.g., supragranular pyramidal neurons), is needed to evaluate this approximation scheme further.

The prospect for developing simplified schemes for predicting contributions to extracellular potentials recorded at the scalp (EEG) seems much better. Here the distances from the neural origin of the electrical signal are sufficiently large for the dipole approximation described in Eq. (8) to give accurate results. This formula describes the contribution to the recorded electrical potentials at a particular electrode contact from a particular neuron receiving synaptic input currents through a particular synapse, information that in principle may be calculated and predicted in large-scale neural network modeling (Jirsa and Haken 1997; Jirsa et al. 2002; Coombes 2005). However, the magnitude and direction of the current dipole moment for the various synaptic inputs, must either be assumed or calculated using multicompartmental modeling, in order for the formula to be workable. The *two-monopole* approximation in Eq. (10) is an alternative. Here the only spatial information needed is the positions of the soma and the active synapse, but the magnitude of the transmembrane current  $I_{tm}$  must still be assumed or calculated using multicompartmental modeling.

A caveat of the present work in the context of predicting EEG signals is that the extracellular conductivity  $\sigma$  has been assumed to be constant. This assumption is clearly violated when the electrical contacts are positioned outside the cortical tissue as in EEG recordings, but our present approach can be generalized to take into account such inhomogeneous electrical media using the same techniques as in the well-established forward modeling of EEG signals from mesoscopic current dipoles (Nunez and Srinivasan 2006).

#### 4.4 Assumptions in forward modeling scheme

Our present LFP forward modeling scheme based on Eq. (1) assumes the extracellular conductivity  $\sigma$  to be the same everywhere ('homogeneous'), the same in all directions ('isotropic'), and also purely ohmic, i.e., no imaginary part from capacitive effects (Nunez and Srinivasan 2006; Logothetis et al. 2007). Finally,  $\sigma$  is assumed to be the same for all relevant frequencies. The validity of this latter assumption is still debated:

while some studies have measured negligible frequency dependence (Nicholson and Freeman 1975; Logothetis et al. 2007), other investigations have suggested otherwise (Gabriel et al. 1996; Bedard et al. 2004, 2006a, b; Bedard and Destexhe 2009). However, if warranted, the present modeling formalism can be generalized to include also a frequency-dependent electrical conductivity  $\sigma(f)$ . More discussion on the assumptions regarding  $\sigma$ , and also ways of generalizing Eq. (1) when they do not apply, can be found in Pettersen et al. (2010).

**Acknowledgements** This work was supported by the Research Council of Norway (eScience, NOTUR). We thank one of the reviewers for bringing relevant literature on human depth-resolved LFP recordings to our attention.

#### References

- Arieli, A. (1992). Novel strategies to unravel mechanisms of cortical function: From macro- to micro-electrophysiological recordings. In A. Aertsen, & V. Braitenberg (Eds.), *Information processing in the cortex*. New York: Springer.
- Bedard, C., Kröger H., & Destexhe A. (2004). Modeling extracellular field potentials and the frequency-filtering properties of extracellular space. *Biophysical Journal*, *86*, 1829–1842.
- Bedard, C., Kröger, H., & Destexhe, A. (2006a). Model of low-pass filtering of local field potentials. *Physical Review E*, *73*, 051911.
- Bedard, C., Kröger, H., & Destexhe, A. (2006b). Does the 1/f frequency scaling of brain signals reflect self-organized critical states? *Physical Review Letters*, *97*, 118102.
- Bedard, C., & Destexhe, A. (2009) Macroscopic models of local field potentials and the apparent 1/f noise in brain activity. *Biophysical Journal*, *96*, 2589–2603.
- Beggs, J. M., & Plenz, D. (2003). Neuronal avalanches in neocortical circuits. *Journal of Neuroscience*, *23*, 11167–11177.
- Berens, P., Keliris, G. A., Ecker, A. S., Logothetis, N., & Tolias, A. S. (2008). Comparing the feature selectivity of the gamma-band of the local field potential and the underlying spiking activity in primate visual cortex. *Frontiers in Systems Neuroscience*, *2*(2). doi:10.3389/neuro.06/002.2008.
- Buzsáki, G. (2004). Large-scale recording of neuronal ensembles. *Nature Neuroscience*, *7*, 446–451.
- Buzsáki, G. (2006). *Rhythms of the brain*. New York: Oxford University Press.
- Carnevale, N. T., & Hines, M. L. (2006). *The NEURON book*. Cambridge, UK: Cambridge University Press.
- Church, P., Leduc, A., & Beique, R. A. (1985). Sensitivity analysis of depth EEG electrodes to dipolar electric sources. *IEEE Transactions on Biomedical Engineering*, *32*, 554–560.
- Coombes, S. (2005). Waves, bumps, and patterns in neural field theories. *Biological Cybernetics*, *93*, 91–108.
- Di, S., Baumgartner, C., & Barth, D. S., (1990). Laminar analysis of extracellular field potentials in rat vibrissa/barrel cortex. *Journal of Neurophysiology*, *63*, 832–840.
- Einevoll, G. T., Pettersen, K. H., Devor, A., Ulbert, I., Halgren, E., & Dale, A. M. (2007). Laminar population analysis: Estimating firing rates and evoked synaptic activity from multielectrode recordings in rat barrel cortex. *Journal of Neurophysiology*, *97*, 2174–2190.

- Freeman, W. J. (1980). Use of spatial deconvolution to compensate distortion of EEG by volume conduction. *IEEE Transactions on Biomedical Engineering*, *27*, 421–429.
- Freeman, W. J., Holmes, M. D., Burke, B. C., & Vanthalo, S. (2003). Spatial spectra of scalp EEG and EMB from awake humans. *Clinical Neurophysiology*, *114*, 1053–1068.
- Gabriel, S., Lau, R. W., & Gabriel, C. (1996). The dielectric properties of biological tissues: III. Parametric models for the dielectric spectrum of tissues. *Physics in Medicine & Biology*, *41*, 2271–2293.
- Godey, B., Schwartz, D., de Graaf, J. B., Chauvel, P., & Liegeois-Chauvel, C. (2001). Neuromagnetic source localization of auditory evoked fields and intracerebral evoked potentials: A comparison of data in the same patients. *Clinical neurophysiology*, *112*, 1850–1859.
- Grech, R., Cassar, T., Muscat, J., Camilleri, K. P., Fabri, S. G., Zervakis, M., et al. (2008). Review on solving the inverse problem in EEG source analysis. *Journal of Neuroengineering and Rehabilitation* *5*, 25.
- Hämäläinen, M., Hari, R., Ilmoniemi, R. J., Knuutila, J., & Lounasmaa, O. V. (1993). Magnetoencephalography theory, instrumentation, and applications to noninvasive studies of the working human brain. *Reviews of Modern Physics*, *65*, 413–449.
- Hines, M. L., Davison, A. P. & Muller E. (2009). NEURON and Python. *Frontiers in Neuroinformatics*, *3*, 1.
- Holt, G. R. & Koch, C. (1999). Electrical interactions via the extracellular potential near cell bodies. *Journal of Computational Neuroscience*, *6*, 169–184.
- Jackson, J. (1998). *Classical Electrodynamics*. NJ: Wiley, Hoboken.
- Jirsa, V. K., & Haken, H. (1997). A derivation of a macroscopic field theory of the brain from the quasi-microscopic neural dynamics. *Physica D*, *99*, 503–526.
- Jirsa, V. K., Jantzen, K. J., Fuchs, A., & Kelso, J. A. S. (2002). Spatiotemporal forward solution of the EEG and MEG using network modeling. *IEEE Transactions on Medical Imaging*, *21*, 493–504.
- Johnston, D., & Wu, S. M.-S. (1995) *Foundations of cellular neurophysiology*, (Chapter 14). Cambridge, MA: MIT Press.
- Katzner, S., Nauhaus, I., Benucci, A., Bonin, V., Ringach, D. L., & Carandini, M. (2009). Local origin of field potentials in visual cortex. *Neuron*, *61*, 35–41.
- Koch, C. (1998). *Biophysics of computation*. New York, NY: Oxford.
- Kreiman, G., Hung, C. P., Kraskov, A., Quiroga, R. Q., Poggio, T., & DiCarlo, J. J. (2006). Object selectivity of local field potentials and spikes in the macaque inferior temporal cortex. *Neuron*, *49*, 433–445.
- Lindén, H., Pettersen, K. H., & Einevoll, G. T. (2008). Frequency scaling in local field potentials: A neuron population forward modelling study *Frontiers in Neuroinformatics. Conference Abstract: Neuroinformatics*, 2008. doi:10.3389/conf.neuro.11.2008.01.026.
- Lindén, H., Pettersen, K. H., Tetzlaff, T., Potjans, T., Denker, M., Diesmann, M., et al. (2009a). Estimating the spatial range of local field potentials in a cortical population model. *BMC Neuroscience*, *10*(1), 224.
- Lindén, H., Potjans, T. C., Einevoll, G. T., Grün, S., & Diesmann, M. (2009b). Modeling the local field potential by a large-scale layered cortical network model. *Frontiers in Neuroinformatics*, Conference Abstract: 2nd INCF Congress of Neuroinformatics. doi:10.3389/conf.neuro.11.2009.08.046.
- Liu, J., & Newsome, W. T. (2006). Local field potential in cortical area MT. Stimulus tuning and behavioral correlations. *Journal of Neuroscience*, *26*, 7779–7790.
- Logothetis, N. K., Kayser, C., & Oeltermann, A. (2007). *In vivo* measurement of cortical impedance spectrum in monkeys: Implications for signal propagation. *Neuron*, *55*, 809–823.
- Lorente de Nó, R. (1947). Action potential of the motoneurons of the hypoglossus nucleus. *Journal of Cellular and Comparative Physiology*, *29*, 207–287.
- Mainen, Z. F., & Sejnowski, T. J. (1996). Influence of dendritic structure on firing pattern in model neocortical neurons. *Nature*, *382*, 363–366.
- Mazzoni, A., Panzeri, S., Logothetis, N. K., & Brunel, N. (2008). Encoding of naturalistic stimuli by local field potential spectra in networks of excitatory and inhibitory neurons. *PLoS Computers in Biology*, *4*, e1000239.
- Miller, K. J., Sorensen, L. B., Ojemann, J. G., & den Nijs, M. (2009). Power-law scaling in the brain surface electric potential. *PLoS Computers in Biology*, *5*, e1000609.
- Milstein, J. N., & Koch, C. (2008). Dynamic moment analysis of the extracellular electric field of a biologically realistic spiking neuron. *Neural Computation*, *20*, 2070–2084.
- Milstein, J., Mormann, F., Fried, I., & Koch, C. (2009). Neuronal shot noise and Brownian  $1/f^2$  behavior in the local field potential. *PLoS ONE*, *4*, e4338.
- Mitzdorf, U. (1985). Current source-density method and application in cat cerebral cortex: Investigation of evoked potentials and EEG phenomena. *Physiological Reviews*, *65*, 37–99.
- Murakami, S., & Okada, Y. (2006). Contributions of principal neocortical neurons to magnetoencephalography and electroencephalography signals. *Journal of Physiology*, *575*, 925–936.
- Nauhaus, I., Busse, L., Carandini, M., & Ringach, D. L. (2009). Stimulus contrast modulates functional connectivity in visual cortex. *Nature Neuroscience*, *12*, 70–76.
- Nicholson, C., & Freeman, J. A. (1975). Theory of current source-density analysis and determination of conductivity tensor for anuran cerebellum. *Journal of Neurophysiology*, *38*, 356–368.
- Normann, R. A., Maynard, E. M., Rousche, P. J., & Warren, D. J. (1999). A neural interface for a cortical vision prosthesis. *Vision Research*, *39*, 2577–2587.
- Nunez, P. L., & Srinivasan, R. (2006). *Electric fields of the brain: The neurophysics of EEG*. Oxford: Oxford University Press.
- Pettersen, K. H., & Einevoll, G. T. (2008). Amplitude variability and extracellular low-pass filtering of neuronal spikes. *Biophysical Journal*, *94*, 784–802.
- Pettersen, K. H., Hagen, E., & Einevoll, G. T. (2008). Estimation of population firing rates and current source densities from laminar electrode recordings. *Journal of Computational Neuroscience*, *24*, 291–313.
- Pettersen, K. H., Lindén, H., Dale, A. M., & Einevoll, G. T. (2010). Extracellular spikes and current-source density. In R. Brette, & A. Destexhe (Eds.), *Handbook of neural activity measurements*. Cambridge, UK: Cambridge University Press.
- Plonsey, R. (1969). *Bioelectric phenomena*. New York: McGraw-Hill.
- Plonsey, R., & Barr, R. C. (2007). *Bioelectricity: A quantitative approach*. New York: Springer.
- Pritchard, W. S. (1992). The brain in fractal time:  $1/f$ -like power spectrum scaling of the human electroencephalogram. *International Journal of Neuroscience*, *66*, 119–129.
- Rall, W. (1962). Electrophysiology of a dendritic neuron model. *Biophysical Journal*, *2*, 145–167.
- Xing, D., Yeh, C.-I., & Shapley, R. M. (2009). Spatial spread of the local field potential and its laminar variation in visual cortex. *Journal of Neuroscience*, *29*, 11540–11549.
- Yvert, B., Fischer, C., Bertrand, O., & Pernier, J. (2001). Localization of human supratemporal auditory areas from intracerebral auditory evoked potentials using distributed source models. *NeuroImage*, *28*, 140–153.